LANDFAST SEA ICE FORMATION AND DEFORMATION

NEAR BARROW, ALASKA: VARIABILITY AND

IMPLICATIONS FOR ICE STABILITY

By

Joshua M. Jones

RECOMMENDED:

Dr. Lewis Shapiro

Dr. Jennifer Hutchings

Dr. Thomas Weingartner

Dr. Hajo Eicken, Advisory Committee Chair

Dr. Paul McCarthy
Chair, Department of Geology and Geophysics

APPROVED:

Dr. Paul Layer
Dean, College of Natural Science and Mathematics

Dr. John C. Eichelberger
Dean of the Graduate School

23 December 2012
Date

LANDFAST SEA ICE FORMATION AND DEFORMATION NEAR BARROW, ALASKA: VARIABILITY AND IMPLICATIONS FOR ICE STABILITY

A

Thesis

Presented to the Faculty
of the University of Alaska Fairbanks

in Partial Fulfillment of the Requirements
for the Degree of

MASTER OF SCIENCE

By

Joshua M. Jones, B.S.

Fairbanks, Alaska

December 2013

Abstract

Climate change in the Arctic is having large and far-reaching effects. Sea ice is declining in annual extent and thinning with a warming of the atmosphere and the ocean. As a result, sea ice dynamic behaviour and processes are undergoing major changes, interacting with socio-economic changes underway in the Arctic. Near Barrow, Alaska, landfast sea ice is an integral part of native Iñupiaq culture and impacts the natural resource extraction and maritime industries. Events known as breakouts of the landfast ice, in which stable landfast ice becomes mobile and detaches from the coast, have been occurring more frequently in recent years in northern Alaska. The current study investigates processes contributing to breakout events near Barrow, and environmental conditions related to the detachment of landfast sea ice from the coast.

In this study, synoptic scale sea level pressure patterns are classified in an attempt to identify atmospheric preconditioning and drivers of breakout events. An unsupervised classification approach, so called Self-Organizing Maps, is employed to sort daily sea level pressure distributions across the study area into commonly observed patterns. The results did not point to any particular distributions which favored the occurrence of breakouts. Because of the comparatively small number of breakout events tracked at Barrow to date (nine events between 2006 and 2010), continued data collection may still yield data that support a relationship between breakout events and large scale sea level pressure distributions.

Two case studies for breakout events in the 2008/09 and 2009/10 ice seasons help identify contributing and controlling factors for shorefast ice fragmentation and detachment. Observational data, primarily from components of the Barrow Sea Ice Observatory, are used to quantify stresses acting upon the landfast ice. The stability of the landfast ice cover is estimated through the calculation of the extent of grounded pressure ridges, which are stabilizing features of landfast ice. Using idealized ridge geometries and convergence derived from velocity fields obtained by coastal radar,

effective grounding depths can be calculated. Processes acting to destabilize or precondition the ice cover are also observed. For a medium-severity breakout that occurred on March 24, 2010, the calculated atmospheric and oceanic stresses on the landfast ice overcame the estimated grounding strength of ridge keels, although interaction with rapidly moving pack ice cannot be ruled out as the primary breakout cause. For another medium-severity breakout that took place on February 27, 2009, the landfast ice was preconditioned by reducing the draft of grounded ridge keels, with subsequent detachment from the shore during the next period of oceanic and atmospheric conditions favoring a breakout. For both of these breakouts, in addition to their potential role in destabilizing the landfast ice by overcoming the ridge grounding strength, current and/or wind forcing on the landfast ice were found to be important factors in moving the stationary ice away from shore.

Table of Contents

List of Figures

Page

List of Tables

Page

Acknowledgements

There are many people who deserve acknowledgement for their encouragement, insight, patience, and help during the completion of my thesis. My time in Fairbanks, Barrow, and everywhere else my work has taken me has been more productive and enjoyable because of them.

First, I would like to thank Dr. Hajo Eicken for giving me the opportunity to do graduate work at the University of Alaska Fairbanks. I am very grateful for the guidance and support you provided, and giving me a chance to gain first hand experience on sea ice in the Arctic. I would also like to thank my graduate committee, Jenny Hutchings, Lew Shapiro, and Tom Weingartner, for helping through difficult problems and providing invaluable feedback throughout my time as a student.

Folks who I have worked extensively with on the ice near Barrow, exploring and discussing interesting ice features, and served as sounding boards for some of my thoughts include Andy Mahoney, Chris Petrich, Matthew Druckenmiller, and Chris Polashenski. Andy and Chris Petrich deserve thanks as well for exhibiting extreme patience during my learning of computer programming.

I would also like to thank other people around the sea ice group and UAF who have helped in various ways. Jeremy Harbeck, thank you for showing me the ropes at UAF and passing on your garden plot. Mette Kaufman for helping me keep track of the lab key and other things I would normally forget. Ellen Craig for keeping tabs on my progress. Jim Kelly, Oliver Dammann, Marc Oggier, Megan O'Sadnick, Olivia Lee, David McAlpin, Alex Sacco, and Arvind C. for being great office mates and getting me to go out for a little entertainment occasionally.

Thanks also to all of the folks in Barrow who have been on the ice with me, sharing their thoughts and stories about the ice and giving me new things to think about. Joe Leavitt, Michael Donovan, Brower Frantz, and Arnie Arey just to name a few. Bryan Thomas deserves special thanks for helping me make sure the radar was always up and

running, and keeping up on the network issues involved. There are also many others involved in Barrow logistic support that deserve thanks as well.

My partner, Hoshi Sugiura, deserves a big thank you for putting up with me during the more stressful periods of graduate school, providing support and keeping me fed. She also had a big job of taking care of the dogs and house by herself while I was away on field work. I also like to thank all of my friends outside of the University for listening to me go on about things you didn't really want to listen to, and for displaying outstanding teammanship. Finally, I would like to thank my family for supporting me and being interested in my work. Especially to my grandfather, Murray Madeen II, who I think was the only one actually paying attention when I explained what I was up to.

The source of my funding during my graduate work should not go unnoticed. I would like to give a big thanks to the Department of Homeland Security's Center for Island, Maritime, and Extreme Environment Security funded my tuition costs and stipend for my entire graduate career at UAF and for that I am very grateful. Funding for other field work opportunities was provided by the National Science Foundation through the Seasonal Ice Zone Observation Network.

Chapter 1
Introduction to Barrow, Alaska and local sea ice conditions

1.1 Introduction

Landfast sea ice is an important seasonal feature of coastal areas in the Arctic. Geologically, landfast ice plays a role in near-shore dynamics of coasts and sediment budgets of coastlines (Reimnitz *et al.*, 1994; Reimnitz and Maurer, 1979). Biologically, the landfast ice cover is an essential habitat for microorganisms, which contribute to primary production in the Arctic Ocean (Horner and Schrader, 1982). Sea ice also serves as a platform from which human activities, such as hunting by native peoples and resource exploration, take place (George *et al.*, 2004; Druckenmiller *et al.*, 2009). While the landfast ice is present along the coasts, it may be used as a surface for on-ice transportation between coastal communities; at the same time it also represents an obstacle to marine traffic (Wilson *et al.*, 2004; Eicken *et al.,* 2009).

Occasionally, during the annual ice cycle of landfast ice formation and disappearance from the coast, so-called breakout events occur, in which landfast ice that seems stably attached to the coast becomes mobile (George *et al*., 2004; Norton and Graves-Gaylord, 2004; Mahoney *et al.*, 2007b; Druckenmiller *et al.*, 2009). These events can be hazardous to people or structures on the landfast ice, stranding persons on moving ice and requiring costly rescue efforts or causing damage to structures. In 1997, a breakout event occurred stranding at least 142 participants in the spring whale hunt on mobile ice, requiring a costly rescue mission (George *et al.,* 2004). The processes involved in the detachment of landfast ice are not well understood (George *et al.*, 2004; Mahoney *et al.*, 2007b), but probably include forces on the landfast ice from offshore winds, interactions between the mobile pack ice and stationary landfast ice, currents or tidal or wind-induced “oscillations” (Shapiro and Metzner, 1989), and abrupt changes in sea level related to tides, currents, and storm surges (George *et al.*, 2004). Grounded

ridges are considered to be stabilizing features of a landfast ice cover, and contribute to the prevention of breakout events (George *et al.*, 2004; Mahoney *et al.*, 2007b; Druckenmiller *et al.*, 2009).

The main focus of this research is to examine the contributing causes to breakout events near Barrow, Alaska. Breakouts are primarily identified through imagery from a land-based marine radar. Using a unique data set, predominantly collected by components of the Barrow Sea Ice Observatory, the strength of the landfast ice cover and the stresses imparted on the ice by environmental conditions before and during a breakout are estimated. Since sea ice moves under the influence of winds, a relationship between breakout events and sea level pressure patterns is also explored.

The next sections provide background information on Barrow, the local seasonal ice conditions, and the Barrow Ice Observatory (Table 1.1). The second chapter employs an artificial neural network to explore a relationship between regional sea level pressure distributions, and thus wind patterns, and landfast sea ice breakout events. The third chapter is focused on in-depth case studies of two breakout events near Barrow. An explanation of general conclusions and future work close out this volume.

1.2 Barrow, Alaska and local sea ice conditions

Barrow, Alaska (Figure 1.1) is the northernmost community in the United States, and is near Point Barrow, which is the farthest north point of contiguous North America. Due to the dominant wind and current conditions in the area, and the orientation of the land-masses, the ice conditions around Barrow are dynamic and sea ice drift regimes differ from other coastal areas in the Arctic (Norton and Graves Gaylord, 2004).

The native Iñupiat people have lived in the Barrow area for over a thousand years, and continue to subsist off the land and ocean today. They have developed an intimate understanding of the sea ice conditions around Barrow, having used the sea ice as a platform for hunting marine mammals. Under the current changing environmental conditions, the Iñupiat in Barrow have observed changes in the local ice conditions

(George *et al.*, 2004; Gearheard *et al.*, 2006; Mahoney *et al.,* 2007b, Druckenmiller *et al.*, 2009). The changes include thinning of the sea ice, a less stable landfast ice cover, less multiyear ice incorporated into the landfast ice, later freeze-up and earlier break-up, and more breakouts during the stable period of the ice season.

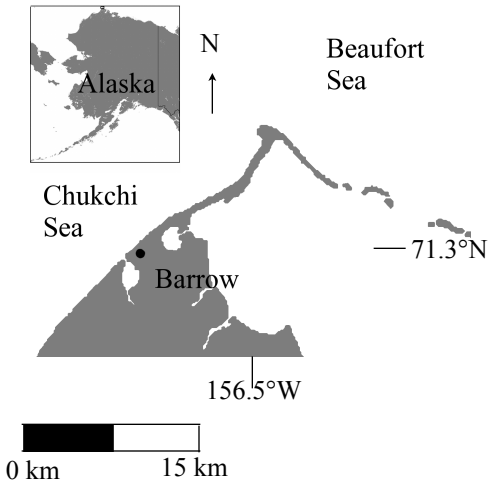

Figure 1.1. Map of Barrow, Alaska and Point Barrow.

Features of coastal ice that are commonly used to define landfast ice include 1) contiguity with the land, and 2) immobility of the ice cover for a specified period of time. Other criteria have been applied to define landfast sea ice, although these two key features are common to most definitions (Mahoney *et al.*, 2005). Mahoney *et al.* (2007a) examined the climatology of the landfast ice cycle in the Barrow area and other parts of the Chukchi and Beaufort Seas in detail, and found the timing of formation and disappearance to depend on atmospheric and oceanic conditions, and coastal morphology (Mahoney *et al.*, 2007a). Landfast ice extensions commonly occur in this area as well. These are expanses of ice that come to rest temporarily along the edge of the landfast ice. Their loss may or may not represent breakout events, depending on the specified time period of immobility in the definition of landfast ice. Mahoney *et al*. (2007a) used 20 days as the time period of immobility to define landfast ice along the Beaufort coast and Chukchi coast based on the timing of satellite imagery used in that study. In the current study, the period of immobility to define landfast ice is seven days, due to better temporal resolution of the data, which is discussed later in Chapter 3. Figure 1.2 shows the different ice zones of the near-shore region during the winter near Barrow.

Typically in recent times, freeze-up begins in late November or early December through in-situ freezing and/or advection of mobile pack ice into shallow coastal waters,

which is later than observations of freeze-up in the 1970's (Shapiro, 1975; Druckenmiller *et al.,* 2009). Since the edge of the pack ice at the end of the summer melt season has been retreating farther north since the 1990's, ice drifts into the coastal area later in the fall months than before, and less multiyear ice drifts near shore throughout the ice season (Drobot and Maslanik, 2003). While some ice may become caught up in the very near-shore, shallow region during the early winter, and some ice may be held against the shore by currents or winds, the early season ice that is stationary is not necessarily stable and may drift away with little forcing. Mahoney *et al.* (2007a) showed that it is typical for the landfast ice to become stably attached to the coast once the seaward landfast ice edge (SLIE) reaches the 18-20m bathymetric region offshore. In the Barrow area, this is generally about 2km from the shore. The 'stable period' of the ice season begins at the end of January or beginning of February, and ends with the onset of thawing at the end of May. Thawing weakens the landfast ice cover and leads into break-up, by melting in place or drifting away under the influence of currents and/or winds. The Chukchi Sea coast near Barrow is usually ice free by late June.

Point Barrow plays an important role in the landfast ice conditions seen along the Northern Chukchi Sea coast. The dominant drift pattern of sea ice in the adjacent Beaufort Sea is clockwise, producing westerly ice drift along the Northern coast of Alaska. This places the Northern Chukchi Sea coast, including Barrow, in the lee of the drift. The result of the typical drift in the Beaufort Sea and orientation of the coast around Point Barrow is a coastal polynya offshore of Barrow. The prevalent north-northeast winds in the area frequently push ice offshore as well (Norton and Graves Gaylord, 2004; Mahoney *et al.,* 2007a). It is this polynya at the edge of the landfast ice that is exploited by the Iñupiat community during the spring bowhead whale migration along the Eastern Chukchi Coast.

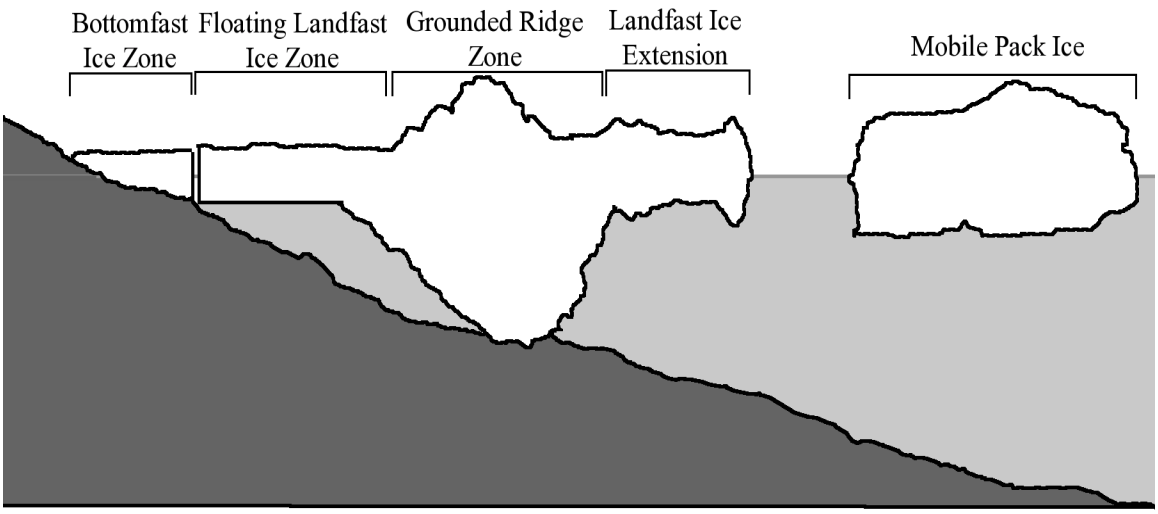

Figure 1.2. Idealized cross-sectional profile of typical landfast ice zones near Barrow, Alaska. Bottom fast ice is separated from floating ice by tide crack. Adapted from Mahoney *et al*. (2007b).

There are also instances during the ice season when the pack ice drifts inshore, closing the coastal polynya. The Iñupiat whale hunters look for these events during the early ice and stable ice periods, as they can result in deformation of the landfast sea ice, and form grounded ridges (Leavitt, personal communication; Mahoney *et al.*, 2004). In-situ deformation and ridge formation is considered an important process in the stabilization of the landfast ice cover near Barrow as a higher number of grounded ridges is observed than would be expected from the distribution of deep first year ridge keels ($\geq$ 20 m) across the Arctic (Mahoney *et al.*, 2007a).

With substantial changes to the sea ice extent and thickness over the past couple of decades and projected into the future (Serreze *et al*., 2007), the Arctic is expecting to experience a major increase in maritime shipping, off- and near-shore resource exploration, and socio-economic changes affecting the political atmosphere of the region (Brigham, 2007). Eicken *et al.* (2009) demonstrated the need for arctic observing networks that provide relevant information to sea ice system stakeholders so they can develop adaptation and mitigation strategies for changing arctic conditions while also

being integrated into addressing important scientific questions. In this context, the monitoring of coastal sea ice dynamics near Barrow, Alaska is not only important in answering pressing scientific questions regarding breakout events in landfast sea ice. The data provides insight into the stability of landfast ice as a platform for various uses, the duration and extent of the landfast sea ice, and the morphology of the near-shore ice. This information can help in making informed recommendations regarding the allowance and regulation of activities in ice covered near-shore regions around the Arctic. An example of such an observation network provided much of the data used throughout the present work.

1.3 The Barrow Sea Ice Observatory

The Barrow Sea Ice Observatory was created to monitor sea ice conditions near Barrow (Druckenmiller *et al.*, 2009). The observatory consists of a mass balance site measuring air temperature, snow depth, sea ice thickness, sea ice temperature profile, water depth below the ice, and in some years, ice or snow albedo. There is also a marine radar unit located on top of one of the tallest buildings in the community of Barrow that observes the ice nearly continuously. Beginning in the 2009-2010 ice season, two oceanographic moorings have been deployed at different distances from the shore to monitor currents, water temperature, conductivity, and water depth. One of these moorings was located under the landfast ice for a portion of the 2009-2010 ice season. A native Iñupiaq whaling captain and local ice expert, Mr. Joe Leavitt, also records ice conditions on a daily basis (Eicken *et al.,* in press 2013). In the Spring, thickness surveys are carried out on the landfast ice, and aerial ice-thickness surveys are performed over the mobile pack ice. Satellite imagery is also an important component of the ice observatory, and provides information on the extent, drift, and types of ice in the area. Table 1.1 describes various components of the observatory.

Table 1.1. Components of the Barrow Sea Ice Observatory, observations made, and spatial and temporal scales of observations. Most observations made throughout the ice season at the interval given, unless otherwise described in the text. Adapted from Druckenmiller *et al.* (2009).

Observatory component	Processes or variables observed	Temporal scale	Spatial scale (m)
Land-based radar	Presence of ice, ice drift, landfast ice extent, beginning of seasonal periods, deformation events, breakout events	minutes	10^1-10^3
Coastal webcam	Presence of ice, deformation events, breakout events, onset of melt, snow on ice	minutes	10^1-10^2
Satellite imagery	Landfast ice extent, beginning of seasonal periods, breakout events, ice type, occurrence and distribution of leads	days	10^1-104
Mass balance site	Air temperature, ice thickness and temperature, snow depth, sea level fluctuations,	minutes	10^0-10^1
Offshore mooring	Current direction and speed, water temperature, depth, conductivity, ice bottom profile	minutes	10^0-10^1
Ice thickness surveys	Landfast ice thickness, near-shore drift ice thickness, surface profile of landfast ice	months	10^1-10^3
Local observations	First ice on coast, deformation events, breakout events, other key events in seasonal ice cycle	days	10^1-10^3

1.4 Thesis overview

The focus of this work is to improve our understanding of landfast sea ice processes near Barrow, Alaska. Using the unique observational data from the Barrow Sea Ice Observatory, and novel techniques of extracting quantitative data from that observational data, the relationship between stresses acting on a landfast ice cover and stabilizing features of the landfast ice cover is explored. This work builds on earlier studies, in particular Shapiro (1975), Mahoney *et al*. (2007b), and Druckenmiller *et al.* (2009).

The second chapter of this work attempts to link breakout events with regional sea level pressure (SLP) distributions. Using an artificial neural network known as a self-organizing map (SOM), characteristic SLP fields are found and compared to SLP fields on the dates of breakout events. The goal is to determine if there is a precursor SLP distribution in the region around Barrow that breakout events are more likely to occur.

Chapter 3 presents two in-depth case studies of breakout events near Barrow. Data from the Barrow Sea Ice Observatory are used to estimate the extent of grounded ridges and stresses on the landfast sea ice leading up to the breakouts. Contributing processes are discussed in this chapter as well. The general conclusions that make up Chapter 4 review the insight gained from this research and what future research can aid in understanding coastal sea ice processes.

Chapter 2

Using self-organizing maps to identify regional weather patterns contributing to landfast sea ice breakouts near Barrow, Alaska

2.1 Introduction

As outlined in the background chapter on landfast sea ice processes and conditions, including breakout events, near Barrow, Alaska, strong wind events and changing wind regimes were implicated as a potential contributing factor in the occurrence of a breakout event. With the identification of 12 breakout events, most of which have occurred during the stable period of the landfast ice cycle according to Mahoney *et al.* (2007a), regional, daily sea level pressure (SLP) distributions are observed for the day of the breakout event as well as the week leading up to the event. The location of the high and low pressure systems provide insight into the direction of the winds in the area, while the proximity of the centers of the highs and lows give an indication of wind strength. The following chapter focuses on employing an artificial neural network known as a Self-Organizing Map (SOM; or Kohonen Map) developed by Kohonen (1995) to identify patterns in the development of SLP distributions observed during breakout events near Barrow, and analyzing specific SLP distributions to identify their potential role in triggering or promoting breakout events.

2.2 Purpose

There are a number of forces that can contribute to breakout events in the Barrow region of the Chukchi Sea (George *et al.*, 2004). Most of these forces are directly or indirectly tied to the sea level pressure (SLP) distribution. For instance, winds are the product of pressure differences in the atmosphere, and winds that blow across landfast ice exert a force that may contribute to a breakout of that landfast ice. Winds also contribute to the movement of pack ice, which may interact with landfast ice, possibly stabilizing or destabilizing the landfast ice. Ocean currents can be driven by winds as well. Movement

of low-pressure systems far away from Barrow near Bering Strait can send storm surges along the Eastern Chukchi coast, which can result in a destabilizing condition by raising the local sea level (George *et al.*, 2004). With this in mind, observing the SLP distribution for the region around Barrow during a breakout event will give an indication of the regional wind regime, and possibly the direction of pack ice motion (beyond the view of the radar) and ocean currents, as well as influencing other factors that can precondition the landfast ice for breakouts.

Previous work by Mahoney *et al.* (2007b) on breakout events along the coast of Barrow concluded that the events are not predictable from local meteorological conditions. In this study, breakout events are considered to be more closely linked to large-scale atmospheric conditions, specifically the daily SLP distributions for the Chukchi, Bering, and Beaufort Seas. Using SOMs to identify characteristic daily SLP patterns in the study region, the hypothesis to be tested is that the SLP distributions for days of breakout events will be the same or very similar.

2.3 Background on self-organizing maps

As an artificial neural network, a self-organizing map is used to identify relationships or patterns in complex data sets. SOMs have been applied in a wide variety of fields including data mining, assessing beer quality, speech and fingerprint identification, and synoptic climatology to name a few (Richardson *et al.*, 2003). A SOM itself is a two-dimensional array of 'nodes', which represent the data that is presented to the SOM software program (Hewitson and Crane, 2002; Richardson *et al.*, 2003; Vesanto *et al.*, 2000). The data can have an infinite number of dimensions or variables, although computation time and memory requirements limit this number. A node in the map can be thought of as a n-dimensional weight vector, where n is equal to the number of dimensions in the data. The number of nodes, and shape of the SOM itself (i.e. 3x4 or 2x6), is either initially chosen by the researcher, or is determined from the number of variables, number of samples, and the amount of generalization of the data that is

acceptable. The number of nodes can be adjusted in subsequent SOM runs based on later frequency analysis of the number of data samples assigned to the previous SOM nodes. The data is then prepared by transforming it into a matrix such that each row corresponds to one data sample and the columns represent the individual variables. For example, in the current study a row in the data matrix corresponds to one daily SLP distribution, while one column contains the SLP data for the same location in the study area. If there are large numerical differences between variables, for example distance measurements in tens of kilometers and velocity measurements in centimeters per second, the data should be normalized along each variable (this is a function available in the SOM software). Since the current study is only using sea level pressure calculations, normalization of the data set is not needed.

Prior to analysis, creation of a SOM requires initialization followed by training. Initialization involves assigning initial values to each weight vector (node) making up the map. The program is initialized either randomly or linearly. Random initialization randomly assigns numbers to the weight vector at each node, such that the vector is the same dimension as the data (number of columns in the data table). Linear initialization assigns initial values to the vectors that are chosen along the greatest eigenvector determined from the data itself.

Training is the next step of the SOM and can be performed as either sequential or batch training. The sequential training method randomly chooses a data sample (row in the table) and presents the sample to each node. The node that is the closest to the data sample based on the minimum Euclidean distance

$$Dist = \sqrt{\sum_{i \to n} (x_i - w_i)^2} \tag{2.1}$$

is deemed the winning node, known as the Best Matching Unit (BMU). Here, x is the randomly chosen data sample, making x_i the ith data value in the data sample being presented to the nodes, w is the weight vector at a node, making w_i the ith value of the

weight vector at the node, and n is the number of dimensions in the data set (columns in the data table). The node is updated to more closely represent the input data sample, and the nodes within a neighborhood are also updated, maintaining the topology of the data set in the SOM. The BMU and nodes within the neighborhood are updated by

$$w(t+1) = w(t) + \alpha(t)h_{ci}(t)[x_i(t) - w_i(t)] \tag{2.2}$$

Here again x is the input data sample and w is the BMU's weight vector. Timesteps are kept track of with t. The influence of an input data sample, h, on the neighborhood, σ, is defined by a Gaussian decay rate

$$h_{ci} = \exp(\frac{-d}{2\sigma^2(t)}) \tag{2.3}$$

and

$$\sigma(t) = \sigma_0 \exp(-\frac{t}{\lambda}) \tag{2.4}$$

where d is the distance between map nodes, σ_0 is the initial neighborhood (the full map), and λ is a constant representing the number of timesteps desired in the SOM training. The neighborhood function, σ, is also a decreasing function of the time steps. The learning rate, α, is again a decaying function

$$\alpha(t) = \alpha_0 \exp(-\frac{t}{\lambda}) \tag{2.5}$$

Hence, the processing can be summarized as follows:

1. A random data sample is presented to each node in the SOM and the distance from the sample to the weight vector at that node is calculated. The weight vector whose distance is the closest is the winning node or BMU.

2. The BMU is updated to more closely match the data sample based on its distance.

3. Nodes within a neighborhood are updated based on a proportion of their distance from the BMU in SOM map units (not their weight vector's distance from the data sample).

4. Repeat these steps while $t < \lambda$.

A depiction of the work flow of the SOM program is shown in Figure 2.1.

The batch method presents the whole data set at once, finding the node that each data sample maps to based on Euclidean distance. The program keeps track of which data samples map to which node. Then, for each node the average of all the data samples that have been mapped to that node is computed, and the neighborhood of that node defined by (2.4) is updated as long as $t < \lambda$. The benefit of using the batch training method is computational, as the listing of where data samples are mapped takes less memory than updating nodes and neighborhoods at every presentation of a data sample to the SOM.

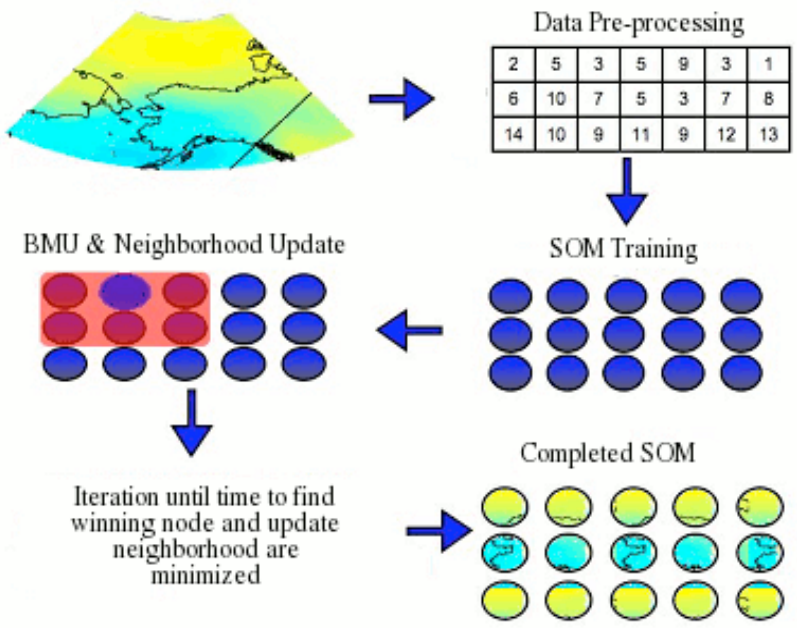

Figure 2.1. Workflow of SOM from SLP field input into algorithm to representative SLP fields located at each node.

There are a number of benefits of using a SOM over other classification methods for the purposes of climate classification. For instance, the output from an SOM is the same as the data that is input and can be physically interpreted, while the output from a principal component analysis is a statistical construct that represents variance within the data set and may not necessarily have a physical interpretation (Reusch *et al.*, 2005). The same is true for finding Characteristic Patterns (CP), as performed in previous work on SLP distributions and breakout events (Mahoney *et al*., 2007a); specific weather patterns cannot be derived from the CPs. For further discussion of the benefits of using SOMs over principal component analysis or other procedures employed in climate classification schemes, see Reusch *et al.* (2005) and Hewitson and Crane (2002).

2.4 Methods and data

Breakout events that took place off the coast of Barrow, Alaska were identified primarily from ice movement and deformation sequences obtained with the sea ice radar that is a component of the Barrow Ice Observatory described in Chapter 1 (Background). The dates for major breakouts that took place before the deployment of the sea ice radar in 2006 were obtained from the available scientific literature (George *et al.*, 2004). For those breakout events identified in the radar imagery, the timing of the event and the direction of ice movement after the breakout can be derived with sufficient accuracy. Breakouts before availability of the radar imagery are typically only tracked if the breakout was relevant to the community's subsistence activities. Table 2.1 shows the dates for the breakouts studied and the source of the breakout information, as well as the direction of motion for the ice that broke away and severity level where available. The majority of breakout events that have been identified are of severity level 2, in which at least half of the landfast ice extent is lost in the breakout event though at least 1 km of ice is left offshore. In the three severity level 1 breakout events, at least 0.5 km of ice was lost and half or more of the pre-breakout extent remained. The single severity level 3

breakout event observed saw most of the landfast ice extent drift away leaving the landfast ice edge less than 0.5 km offshore.

The sea level pressure fields used in this study derive from the Reanalysis I products of the National Center for Environmental Prediction/National Center for Atmospheric Research (NCEP/NCAR) as provided by the NOAA/OAR/ESRL PSD, Boulder, Colorado, USA, from their Web site at www.esrl.noaa.gov/psd/ (Kalnay *et al*., 1996). The SLP data are daily averages of sea level pressure from January 1, 1948, to December 2010 covering the area from 45˚N to 90˚N and 140˚E to 260˚E (100˚W; Figure 2.2). The values in any daily SLP field represent the average sea level pressure for a 2.5°x2.5° area, calculated from the NCEP/NCAR reanalysis algorithm. Therefore, each daily field is represented by a 49x19 grid of SLP values.

The SOM program used in this study is the SOM Toolbox 2.0 for Matlab that is freely available from the Laboratory of Computer and Information Science at the Helsinki University of Technology (www.cis.hut.fi/somtoolbox/). The preprocessing of the data for input into the SOM program required the creation of a data table from the 23011 daily SLP fields. Each row in the table represents a single daily SLP field, each column corresponds to one SLP value from that day. The resulting data table consisted of 23011

Table 2.1. List of breakout events near Barrow, Alaska

Date	Breakout Observation	Breakout Direction (Severity Level)
May 17, 1997	George *et al*., 2004	
Dec 11, 2001	George *et al*., 2004	
Mar 17, 2002	George *et al*., 2004	
Jan 31, 2007	Radar	SW (1)
Feb 11, 2007	Radar	SW (2)
Mar 31, 2007	Radar	N/NE (2)
May 28, 2007	Radar	N/NE (1)
Jan 20, 2008	Radar	NE (3)
Mar 29, 2008	Radar	N/NE (1)
Feb 5, 2009	Radar	SW (2)
Feb 27, 2009	Radar	NW (2)
Mar 24, 2010	Radar	SW (2)
Apr 28, 2010	Local/Satellite Observation	

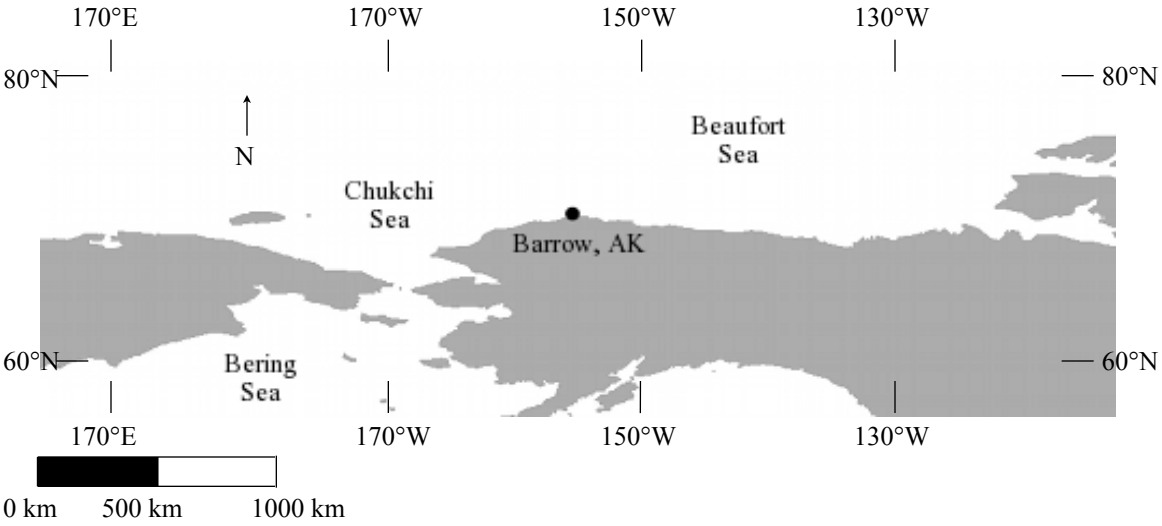

Figure 2.2. General map of study area used in SOM analysis.

rows with 931 columns each. No normalization of the data was needed because all variables (columns) are SLP values and of essentially the same magnitude. A heuristic formula within the SOM Toolbox is used to determine the number of nodes and side lengths for the final map. Initially, the SOM Toolbox chose over 260 nodes, which is quite large. In this case, the program can reduce the number of nodes to one fourth of the heuristically determined number of nodes, which brought the total number of nodes to 66 in this study. The side lengths are set by maintaining the ratio of the two largest eigenvalues of the data set. The map in this study was set to be 11x6. The SOM was then initialized using the linear method, and trained using the batch method. This approach reflects conclusions drawn from measurements of quantitative and topographic error associated with SOMs that have been created with different combinations of initialization and training methods, and will be discussed in the results section. Using different labeling techniques for the input data, the nodes corresponding to SLP fields on the day of a breakout event and the seven days prior were determined.

2.5 Results

As a first step in the analysis, the quality of the SOM was assessed using the errors associated with alternative options for generating the SOM. Specifically, the quantization error and topographic error for each combination of initialization and training methods are given in Table 2.2. Quantization error is the average Euclidean distance between a map node and all individual SLP fields mapped to that node (BMU), and then averaged over all nodes. Quantization error is a measure of map resolution. Topographic error is the percentage of daily SLP fields whose second BMU in the SOM is not adjacent to BMU, or node the field is mapped to. This is a measure of how well topology was preserved in the SOM. The magnitude of the quantization errors between the four combinations are the same, and the values are quite similar, with random initialization showing increased values over linear initialization. Batch training values are slightly higher than those of sequential training, especially for the random initialization. The topographic errors are quite low as well, ranging from 4.5% to 0.5%. The linear initialization and batch training methods show topographic errors that are an order of magnitude lower than all other methods, while this combination also has only slightly higher quantitative errors than the method with the lowest value of these errors. Therefore, the SOM initialized and trained with the linear and batch methods are used for subsequent analysis in this study.

The SOM nodes are shown in Figures 2.3a and 2.3b. The number in the upper left corner of each is the node number, which will be used in reference to a specific node. The number in the upper right of each node is the percentage of actual SLP fields that

Table 2.2. Error estimates for different SOM settings

SOM Training/ Initialization	Quantization Error (hPa)	Topographic Error (%)
Batch/Linear	148.26	0.50
Batch/Random	156.70	4.50
Sequential/Linear	145.36	1.20
Sequential/Random	145.60	2.60

mapped to that node. Table 2.3 lists the trajectories of the SLP distributions through the SOM nodes. Refer to Figures 2.3a and b for visual inspection of the SLP distribution for the days leading up to, including the day of, the breakout event.

There is no clear pattern in SLP distributions during breakout events, nor is there a common trajectory of SLP fields. However, two-thirds of the trajectories seem to show an increase in sea level pressure gradient around the Barrow area for two to three days leading up to the breakout event. Some of the trajectories do not explicitly show an increase in gradient, as the pre-breakout days are mapped to the same node as the breakout. This is due to the generalization of the SLP pressure fields represented at each map node. In these cases, the actual SLP distributions for those days are used to visually determine if an increase in the pressure gradient around Barrow occurred. Table 2.4 lists the sea level pressure gradients for the day of the breakout events, as well as the two days prior. Instances in which the pressure gradient is increasing leading up to the breakout are highlighted yellow. Since Barrow is near the northern border of the 2.5°x2.5° grid cell in the NCEP/NCAR Reanalysis data, the grid cell that is just north of Point Barrow is included in this analysis as well. In some cases, the SLP gradient in the northern grid cell is increasing, while the gradient for the grid cell that contains Barrow is decreasing.

Table 2.3. Daily SLP trajectories through SOM nodes prior to breakout events.

Date of Breakout	Breakout Node	1-day prior	2-days prior	3-days prior	4-days prior	5-days prior	6-days prior	7-days prior
May 17, 1997	43	43	42	32	43	32	33	33
Dec 11, 2001	2	2	2	8	19	20	9	19
Mar 17, 2002	62	62	63	62	62	8	9	9
Jan 31, 2007	22	10	9	8	8	8	2	2
Feb 11, 2007	9	63	33	33	33	33	9	33
Mar 31, 2007	63	63	62	56	34	34	12	1
May 28, 2007	38	39	29	29	30	52	52	60
Jan 20, 2008	62	63	63	63	62	3	2	8
Mar 29, 2008	63	64	65	65	66	66	66	66
Feb 5, 2009	11	11	22	33	43	30	18	58
Feb 27, 2009	56	56	56	61	61	62	64	59
Mar 24, 2010	33	44	44	44	44	44	62	63
Apr 28, 2010	18	18	19	19	19	40	28	16

Table 2.4 also shows the opposite direction of the sea level pressure gradient for the same two grid cells. The opposite direction of the calculated gradient is given, since the pressure gradient force is directed from areas of high pressure to low pressure. Due to the Coriolis force, the air flow is deflected to the right. Once the pressure gradient force and the Coriolis force are in balance, geostrophic flow is present with winds moving parallel to the SLP isobars. Near the surface of the Earth, however, friction reduces the Coriolis force and the wind is directed more along the pressure gradient, and local winds can deviate from the direction of the pressure gradient and Coriolis forces from interaction with local topography. Sea ice moves about 8° to the right of the geostrophic wind without the influence of the coast or internal stresses (Thorndike and Colony, 1982), which is not the case near Barrow. As a rule of thumb for this area, ice is assumed to move about 30° to the right of the local wind (Shapiro and Metzner, 1989).

2.6 Discussion

The results from the initialization and training of the SOM are similar to those of Cassano *et al*. (2011), who analyzed sea level pressure distributions for an area slightly smaller than the current study, and defined the self-organizing map to be 5x7, for 35 map nodes. While the SOM trained in the Cassano *et al*. (2011) study captures less of the variability seen in SLP distributions over the Alaskan region, none of the SLP distributions observed in the previous study are absent from the current study's SOM. A direct comparison of magnitudes of SLP between nodes is not possible since the Cassano *et al*. (2011) study used SLP anomalies from the daily mean as input into the SOM.

The SOM can also be shown to capture the variability of SLP distributions that produce the various weather conditions observed in the study region by comparing the SOM to an SOM with fewer nodes. Figure 2.4 displays a 4x6 SOM with 24 nodes, with the area of daily SLP distributions slightly smaller as well, 55˚N to 85˚N and 165˚E to 245˚E (115°W), for the same time period of January 1, 1948 to December 31, 2010. The 4x6 SOM is dominated by a north-south pressure gradient regime, resulting from the

greater generalization of SLP distributions to only 24 patterns and the restricted spatial domain. The 6x11 SOM used for analysis in this study has nodes whose SLP distribution would produce northerly/southerly winds in the Barrow area. The range of SLP values in the 6x11 SOM is also higher, due to less generalization needed in a larger SOM.

The NCEP/NCAR Reanalysis data, provided on a 2.5°x2.5° grid, necessarily decreases the physical dimensions of grid cells farther to the North due to the convergence of lines of longitude, thereby introducing a systematic bias towards data from the northern parts of the study area. This was accounted for by interpolating the latitude/longitude grid of SLP data onto a polar stereographic grid. Another source of error that is found in the Reanalysis data deals with the number of atmospheric measurement locations in the remote areas of the study domain through time. In the Northern portion of the domain, there may be few if any measurement sites, especially farther from the coasts. While there is no available data for certain periods of time and regions from 1948 to 2010, the reanalysis project assimilates a model and observations to estimate the state of the atmosphere. Please see Kalnay *et al.* (1996) for a more in depth discussion of the NCEP/NCAR Reanalysis project.

The SLP distributions for the days of breakout events in Barrow did not map to a single SOM node, nor to one region of the SOM. Also, the trajectories of the SLP distributions leading up to breakout events were not similar between all cases. A visual inspection of the nodes for the days leading up to a breakout shows that there was increasing pressure gradient, regardless of direction, for six of the thirteen of the cases. Since the SOM generalizes the SLP patterns that are visualized at each node, the magnitude and actual direction of the SLP gradient cannot be determined from the map itself. There are also some cases in which the day prior to the breakout is mapped to the same node as the day of the breakout. In these cases, an increase in SLP gradient cannot be seen. For these reasons, the actual SLP distribution for the day of the breakout event,and the two days before, were used to calculate the magnitude and direction of the SLP gradient for the Barrow area. The results from these calculations increase the

number of breakout events with increasing SLP gradients from six to eight, or about 61.5% of the breakout cases. Considering the SLP trajectories through the SOM of an entire month before these breakout events, there were at least two instances of an increasing SLP gradient in the Barrow area for each case. The increasing SLP gradients during the month prior to the event were of at least the same (SOM) magnitude as the increasing gradient leading to the breakout, although for five of these cases there was at least one period during the prior month before the breakout that the (SOM) magnitude of the gradient increase was larger than the gradient increase directly before the breakout.

In the cases in which the SLP gradient is increasing, and the direction of the breakout can be determined from animations of radar imagery, a total of six cases, four of the directions of breakout motions are consistent with the pressure gradient and associated turning angle for ice motion. These breakouts are those of January 31, 2007, February 11, 2007, February 5, 2007, and March 24, 2010. In the other two instances, the motion of the broken-out ice does not follow the surface pressure gradient and related turning angle, January 20, 2008, and February 27, 2009.

It appears that there may be some clustering of breakouts in the SOM in the upper right corner, around node 21 possibly, and around nodes 62 and 63. Considering the dates of the breakouts that occurred around these possible clusters, there is no discernible relationship between the SLP distribution and the time of year the breakout occurs. That is, breakouts which make up the possible clusters occurred throughout the ice season. There are not enough breakout examples to conclude that breakouts occur more often under SLP distributions similar to those at nodes ~21 and ~63 at this time.

2.7 Conclusions

Based on the results from the SOM analysis of sea level pressure fields and the fields' trajectories though time leading up to a breakout event near Barrow, Alaska, there is no SLP pattern or development of the patterns that exhibits any direct correlation or potential causal relationship with the breakout events. Using a ground-based radar

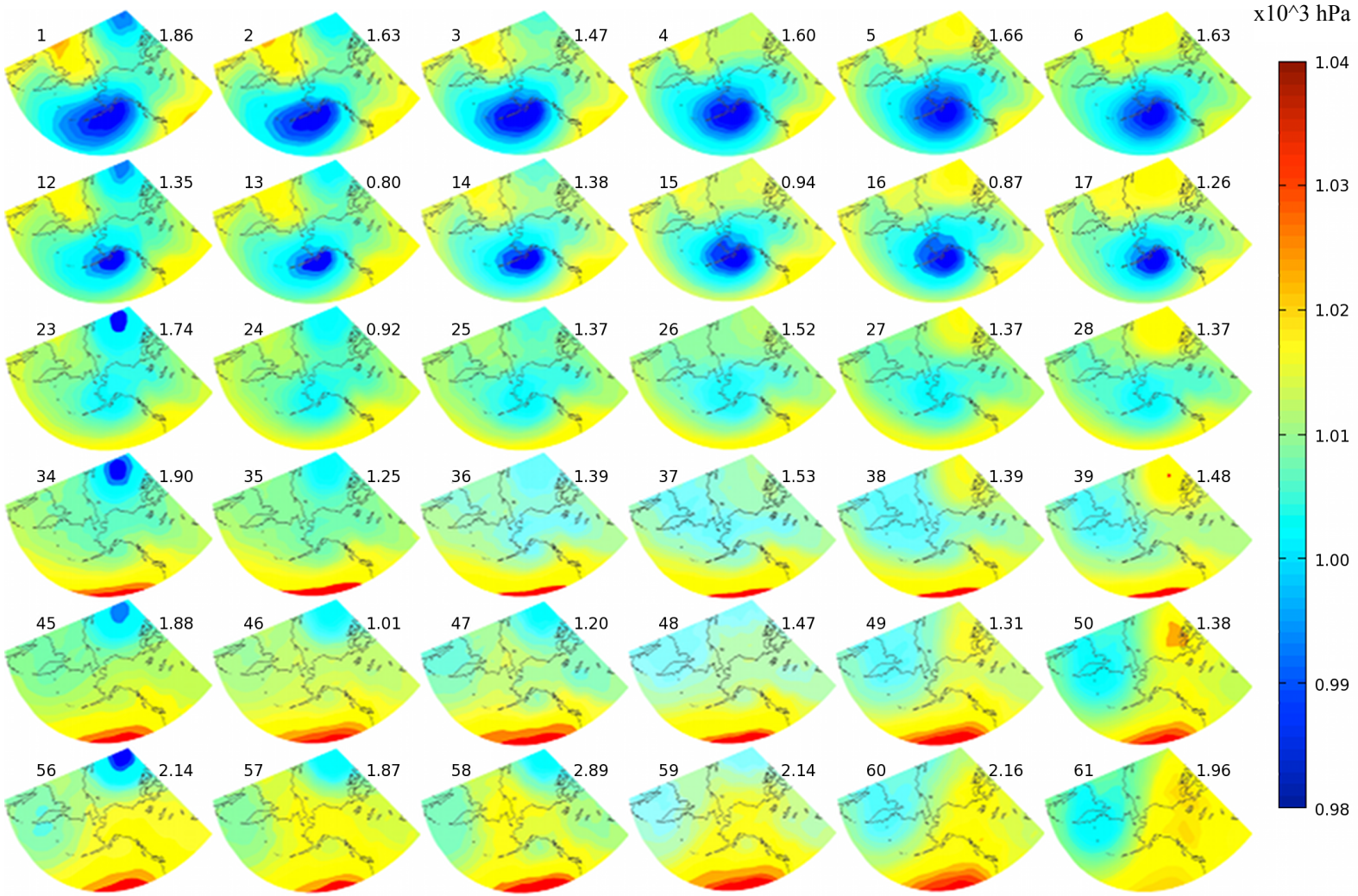

Figure 2.3a. Left side of 11x6 SOM. The node number is in the upper left of each SLP field. The percentage of daily SLP distributions that mapped to each node is on the upper right.

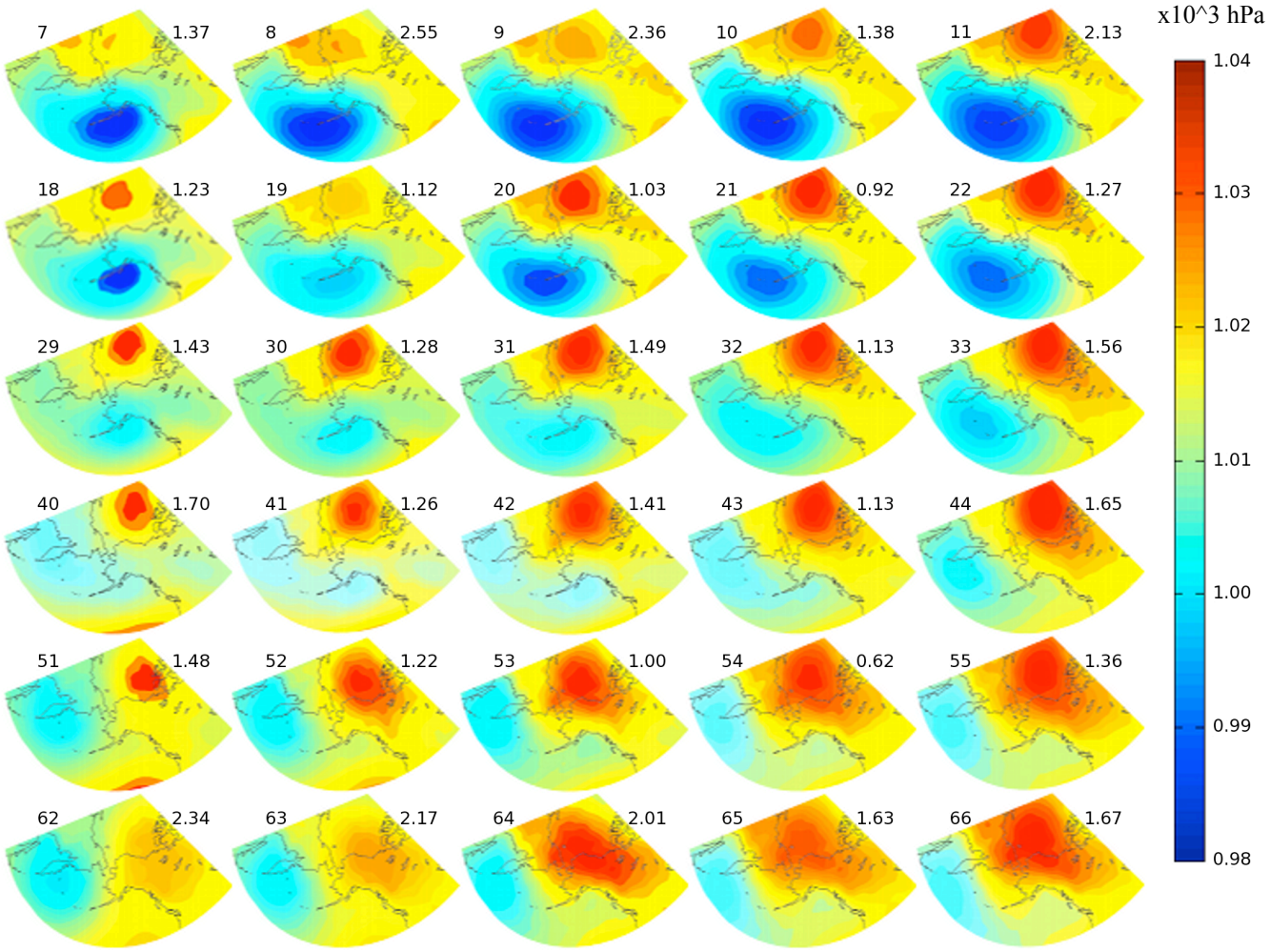

Figure 2.3b. Right side of 11x6 SOM. The node number is in the upper left of each SLP field. The percentage of daily SLP distributions that mapped to each node is on the upper right.

Table 2.4. SLP gradient magnitudes (hPa/2.5°) and directions.

Date	Barrow's Grid Cell		Grid Cell North of Barrow	
	SLP Gradient Magnitude (hPa/2.5°)	Down-Gradient Direction (° from N=0°)	SLP Gradient Magnitude (hPa/2.5°)	Down-Gradient Direction (° from N=0°)
May 15, 1997	0.510	191.3	0.692	164.1
May 16, 1997	0.691	229.4	0.817	156.6
May 17, 1997	1.220	223.5	2.153	195.5
Dec 9, 2001	3.927	194.0	4.228	182.0
Dec 10, 2001	4.181	197.4	4.945	183.6
Dec 11, 2001	3.295	194.5	5.089	187.1
Mar 15, 2002	2.664	223.3	2.475	212.4
Mar 16, 2002	4.282	230.2	3.348	224.8
Mar 17, 2002	2.115	98.8	1.885	91.1
Jan 29, 2007	0.646	200.7	3.150	258.3
Jan 30, 2007	5.646	190.8	7.479	149.6
Jan 31, 2007	4.836	184.7	9.276	186.6
Feb 9, 2007	1.951	244.8	0.689	179.7
Feb 10, 2007	2.535	193.1	0.910	181.9
Feb 11, 2007	5.143	203.8	4.671	191.2
Mar 29, 2007	1.606	152.6	4.445	170.6
Mar 30, 2007	1.847	154.3	3.483	165.0
Mar 31, 2007	1.577	259.4	1.384	111.2
May 26, 2007	4.397	175.8	5.198	183.1
May 27, 2007	2.808	166.9	4.822	184.0
May 28, 2007	1.570	162.8	3.529	185.1
Jan 18, 2008	3.412	188.4	3.514	190.9
Jan 19, 2008	2.047	259.9	2.844	209.5
Jan 20, 2008	5.283	137.4	3.014	118.4
Mar 27, 2008	1.523	174.0	2.729	189.7
Mar 28, 2008	1.231	137.0	2.340	179.8
Mar 29, 2008	0.381	156.8	0.592	220.6
Feb 3, 2009	1.885	185.8	2.216	178.7
Feb 4, 2009	3.203	187.6	2.199	185.2
Feb 5, 2009	6.327	183.5	5.111	183.8
Feb 25, 2009	1.556	135.5	3.143	159.3
Feb 26, 2009	3.774	163.9	0.500	180.1
Feb 27, 2009	0.525	270.0	2.758	157.1
Mar 22, 2010	6.601	187.1	6.422	190.4
Mar 23, 2010	8.075	183.5	5.865	185.3
Mar 24, 2010	9.452	186.0	9.352	185.5
Apr 26, 2010	6.188	174.6	3.680	183.1
Apr 27, 2010	6.599	175.1	8.395	177.2
Apr 28, 2010	3.861	175.8	6.800	179.4

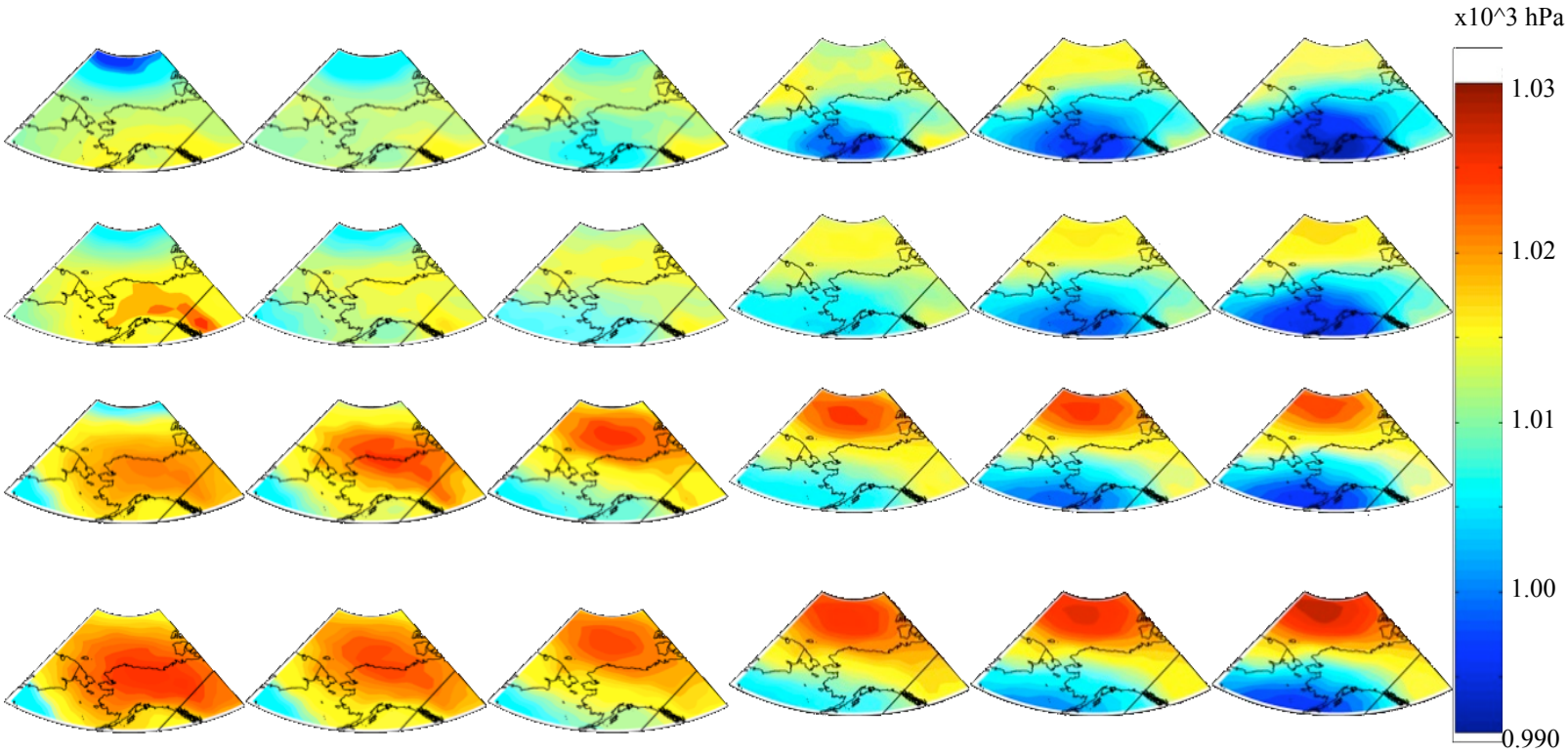

Figure 2.4. A smaller, 6x4, sOM. This SOM does not capture the variability in SLP distributions observed for the region as well as the 11x6 SOM used for this study.

system to observe near-shore ice movement greatly aids in the identification of breakout events, and allows the direction of the breakout motion to be determined. This is a great benefit over relying on local accounts or satellite observations of breakout events, as nearly the exact time of the breakout can be determined. Based on analysis of this radar data, there seems to be no consistent relationship between regional sea level pressure changes and direction of ice movement and hence application of surface stress during a breakout event.

This study is limited by the number of breakout examples observed in the sea ice radar imagery. Collection of a longer time series at high resolution will allow more breakouts to be observed in detail, from which stronger statistical analysis can take place. From these results, however, it appears that a more in depth study of the conditions leading up to and during a breakout event are needed. For instance, in two cases the breakout motion is nearly directly upwind, based on the regional sea level pressure gradient. While local conditions may not be exactly as the regional SLP distribution indicates, the regional SLP gradient still provides a good indication of local, near-surface conditions (Cassano *et al*., 2011). As the breakout motion was obviously not near the down-gradient direction, a stress applied by the ocean at the base of the ice cover is implicated in the breakout event. For this region, the prevailing wind direction is from the Northeast, while the average coastal current in the Barrow area is to the North/Northeast (Weingartner *et al.*, 1998). Finally, since there were similar SLP conditions and onshore mobile ice trajectories visible in the radar before breakout events, an examination of the development of the landfast ice cover prior to the breakout event may provide clues as to why the breakout occurs when it does. These topics are the focus of the next section of this thesis, performing in-depth case studies on two of the breakout events used in the SOM analysis.

Chapter 3

Two case studies of landfast sea ice breakouts near Barrow, Alaska

3.1 Introduction

Landfast sea ice is a seasonal, although important, feature along the coast near Barrow, Alaska. The formation of a stable landfast ice cover takes place throughout the ice season with offshore ice drifting into coastal waters, and ice pressure ridges grounding on the sea floor . There are two ways in which ridges become grounded, by drifting into or being built in shallow water (Mahoney *et al*., 2007b). In either case, it is these grounded pressure ridges and the atmospheric and oceanic forces controlling their formation and decay that ultimately cause the stabilization of a landfast ice cover near Barrow.

The same forces that give rise to the presence of stabilizing grounded ridges can work to dislodge a stable landfast ice cover, either directly or indirectly. Currents and/or winds can exert enough force to break ridge keels or dislodge the keels from the gouge created during the grounding process. Drifting ice can come into contact with landfast ice and knock it loose in some instances. Other factors can also precondition the landfast ice for a breakout. A rise in sea level can lift the ridge keels out of their gouges, while a drop in sea level could cause the ridge keel to shorten under the added weight. The exact conditions that lead up to and contribute to a breakout are not well known, and difficult to measure, as are the extent and strength of grounded ridges opposing breakout forces.

In this chapter, two breakout events are the subjects of case studies aimed at identifying the causes of the breakouts. The first breakout being discussed occurred on February 27, 2009 while the second occurred on March 24, 2010. These breakouts were chosen based on the time of year the breakout occurred, availability of environmental data, severity of the breakout, and possible relevance to local landfast ice users. After a discussion of relevant background information, the data collected and methods, each case study begins with a description of the formation of the landfast ice before the breakout

occurred. The extent of grounded ridges is estimated using novel radar image processing techniques. The atmospheric and oceanic conditions leading up to and during the breakout events are then discussed, with an estimation of the force imparted on the landfast ice cover. The final section compares the sequence of events contributing to the two breakouts.

3.2 Background

3.2.1 Drift and dynamics of sea ice

Stresses applied to the ice's upper and lower surfaces, by wind and ocean currents, cause the ice to drift. Due to its comparative homogeneity and great lateral extent at the scale of acting forces, floating sea ice can be treated in two dimensions (Coon *et al.*, 1974; Hibler, 1986; Leppäranta, 2005). The third dimension of sea ice, its thickness, is accounted for in the following equations by integrating mass and momentum through the thickness (Gray and Morland, 1994). The drift of sea ice is determined by the forces described in the equation for momentum balance

$$\frac{D(m\mathbf{u})}{Dt} = -mf_c\mathbf{k}\times\mathbf{u} + \tau_a + \tau_w - m\hat{g}\Delta H + \nabla\cdot\sigma_{ij} \tag{3.1}$$

where m is the mass per unit area of ice, $\mathbf{u}$ is the ice velocity in the x_1 direction (Figure 3.1), D/Dt denotes the material or substantive derivative of the mass times ice velocity ($\partial/\partial t+\mathbf{u}\cdot\nabla$), f_c is the Coriolis parameter given as

$$f_c = 2\Omega\sin\vartheta \tag{3.2}$$

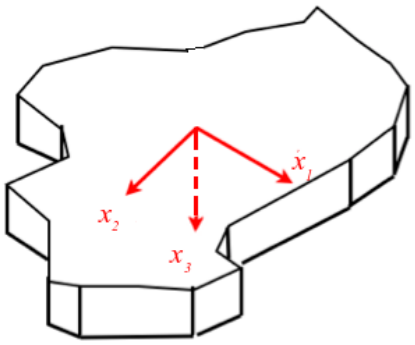

Figure 3.1. Representative ice floe with coordinate system displayed.

with Ω=7.292x10^{-5} s^{-1}, and ϑ being latitude. In Equation 3.1, **k** is a unit normal vector in the x_3 direction, τ_a is the stress from wind moving over the ice surface, τ_w is the water stress from currents under the ice, $mg\Delta H$ is the force due to sea surface tilt with g as gravitational acceleration in a true vertical/horizontal coordinate system and H is the dynamic height of the sea surface. The term $\nabla \cdot \sigma_{ij}$ represents the internal forces within the ice with σ_{ij} as the vertically integrated deviatoric stress ($\rho_{ice} z_i 2g\delta_{ij}$; where ρ_{ice} is the ice density, z_i is the ice thickness, and δ_{ij} is the Kronecker delta operator) (Feltham, 2008).

The air and water stresses on the ice are defined as

$$\tau_a = c'_a U_a \tag{3.3}$$

and

$$\tau_w = c'_w U_w \tag{3.4}$$

where U_a and U_w are the wind velocity at 10m and current velocities, respectively. The drag coefficients, which are approximated by quadratic boundary layer laws (McPhee, 1986; McBean, 1986), c'_a and c'_w, are defined as

$$c'_a = \rho_a c_a U_a \tag{3.5}$$

and

$$c'_w = \rho_w c_w U_w \tag{3.6}$$

with ρ_a and ρ_w being the densities of air and water, and c_a and c_w being the dimensionless drag coefficients. The drag coefficient for the ice exposed to the winds depends on the roughness of the ice surface, and includes skin and form drag

$$c_a = c_{10} + (c_f \bar{h}_s N/2) \tag{3.7}$$

where c_{10} is the skin drag (0.00190 for arctic ice), c_f is form drag (0.300 for first year ridges), $\bar{h}_s$ is the mean sail height, and N is the average number of ridges in the downwind direction (Banke and Smith, 1973). Values for c_a can range from 0.00150 for very smooth first year ice to 0.00800 for extremely rough multi-year ice (Guest *et al*., 1994). Values for rough first year ice and extremely rough first year ice, which are typical ice conditions near Barrow, are 0.00310 and 0.00420, respectively. Likewise, the drag coefficient for the ice-water interface depends on the roughness of the surface in contact with the water, ranging from 0.00780 for smooth floes (Reynolds *et al*., 1985) to 0.0200 for ice in the central Arctic (McPhee, 1979). A ratio of c_a/c_w of 0.24 was suggested by Leppäranta (2005). So, considering a very rough landfast ice cover near Barrow, and taking a value of 0.0042 for c_a, the value for c_w would be 0.0175. Substituting Equations (3.5) and (3.6) into Equations (3.3) and (3.4) yields

$$\tau_a = \rho_a c_a U_a^2 \tag{3.8}$$

$$\tau_w = \rho_w c_w U_w^2 \tag{3.9}$$

There are many assumptions associated with the momentum balance equation for sea ice. This equation assumes that the ice field is an isotropic continuum. The area of ice being moved is also subject to an averaging of surface roughness in the drag coefficients used. These are reasonable assumptions considering the difficulty in measuring the surface roughness and anisotropies of a large area of ice.

Stresses on the landfast ice due to shear with the atmosphere and ocean at the air-ice and ocean-ice interfaces are

$$F_a = L_{LFI}\tau_a \tag{3.10}$$

and

$$F_w = L_{LFI}\tau_w \tag{3.11}$$

where L_{LFI} is the distance over which the wind or current is acting on the landfast ice, i.e., the fetch. Substituting Equations (3.8) and (3.9), and inserting the drag coefficients gives

$$F_a = L_{LFI}\rho_a c_a U_a^2 \tag{3.12}$$

$$F_w = L_{LFI}\rho_w c_w U_w^2 \tag{3.13}$$

These are the effective stresses that work to move sea ice, and act upon stationary landfast ice.

3.2.2 Breakout events: Ridge failure

When considering the impact of grounded ridges on the stability of the landfast ice cover by grounded ridges, the anchoring strength of the grounded ridges is dependent upon the coupling of blocks in the ridge keel to the sea floor, the effective strength of block contacts in the unconsolidated portion of the ridge keel, and the strength of the sea floor sediments. If a ridge drifts into the near-shore zone, and the ridge keel gouges into the the sea floor, the effective strength of the frictional coupling may depend on the direction of the destabilizing forces acting on the ridge. For a wind or current stress forcing the ice in the opposite direction of its initial contact with the sea floor, the gouge walls may not provide the same magnitude of friction or constraint as that of the ridge being pushed in

any other direction. Therefore, the stability derived from frictional coupling with the sea floor may be difficult to estimate.

Mahoney *et al.* (2007b) described the shear stress from frictional coupling as

$$\sigma_{sb} = \frac{W_g c_f}{A_g} \tag{3.14}$$

where W_g is the weight of the ridge with buoyancy accounted for, c_f is the coefficient of friction between the sea bed and the ridge keel, and A_g is the area of the ridge keel making contact with the sea bed. For static friction, a value of 0.5 for c_f was given by Shapiro and Metzner (1987), who dragged smooth ice blocks across a gravel beach near Barrow. Druckenmiller (2011) developed a system of equations for describing the shear strength at the sea floor-ridge keel interface, with the weight of the ridge in terms of ridge geometry, assuming a unit length of the ridge and that the keel is grounded and therefore the same depth as the water

$$W_g = \frac{\rho_w g (H_k - w_g)^2}{\tan\alpha_k} \tag{3.15}$$

where ρ_w is the density of the water, g is the gravitational constant, H_k is the keel depth of an idealized triangular ridge keel, w_g is the depth of the water, and α_k is the slope angle of the keel (see Figure 3.2). Also, assuming that the area of the ridge in contact with the sea floor, A_g, applies to the width of the ridge keel at the water depth w_g, which would also be the keel depth if no significant gouging takes place, the area in contact can be expressed as a length (assuming unit length of the ridge)

$$l_g = \frac{A_k \tan\alpha_k - w_g^2}{w_g \tan\alpha_k} \tag{3.16}$$

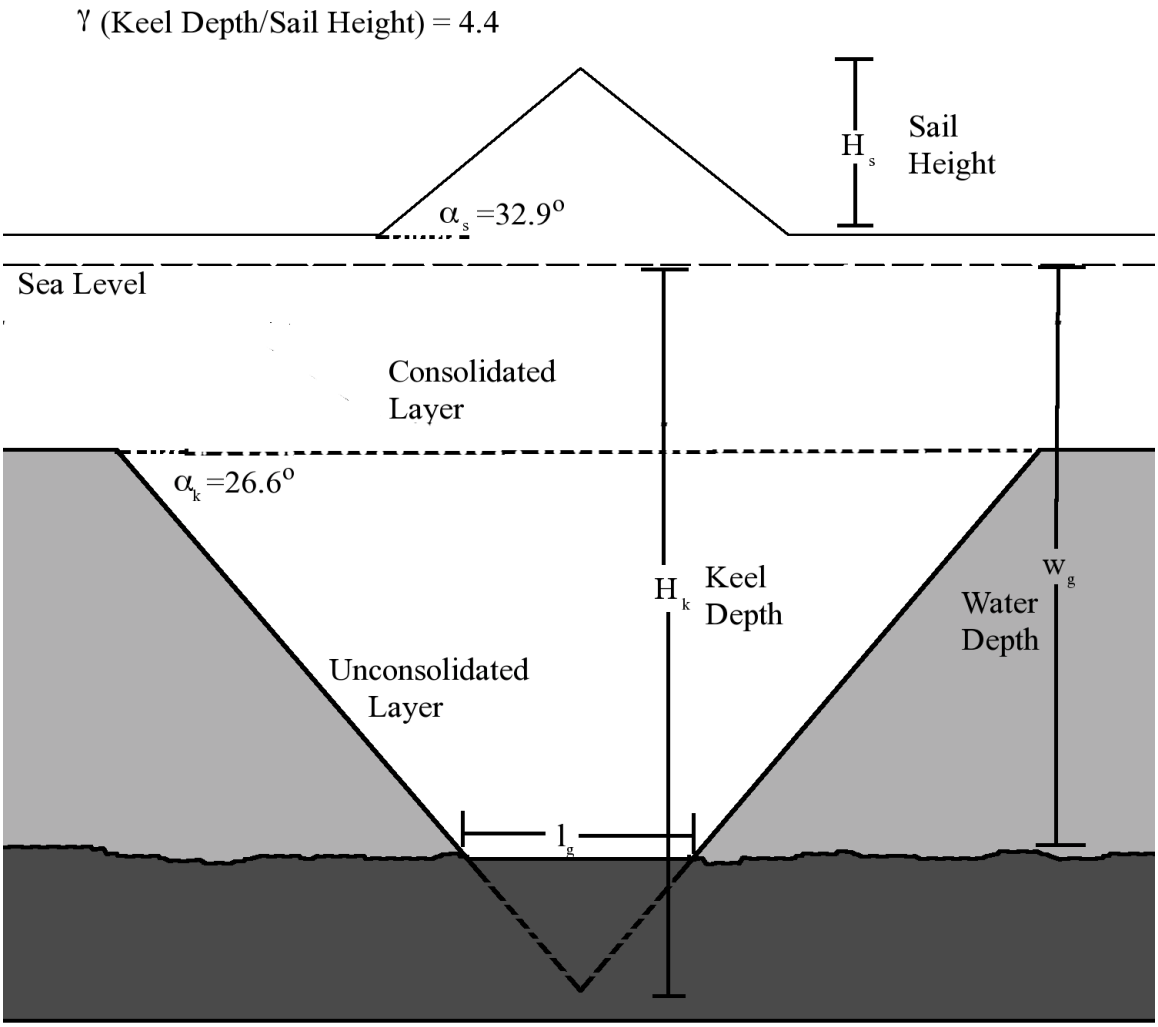

Figure 3.2. Idealized cross section of grounded pressure ridge. Ridge geometry variables and relevant ratios are given in the figure. Average values that are given are from Timco and Burden (1997), from which the figure is adapted.

where A_k is the cross-sectional area of the ridge keel. Substituting Equation (3.15) and (3.16) into Equation (3.14) gives

$$\sigma_{sb} = \frac{\rho_w c_f g w_g (H_k - w_g)^2}{A_k \tan\alpha_k - w_g^2} \tag{3.17}$$

Furthermore, the total effective frictional stress provided by all of the grounded ridges in a landfast ice cover is given by

$$F_{sb} = W_g c_f n_g \tag{3.18}$$

with n_g being the number of grounded ridges. With the substitution of W_g from Equation (3.15)

$$F_{sb} = \frac{c_f n_g \rho_w g \overline{D}_g}{\tan\alpha_k} \tag{3.19}$$

where the average D_g is defined as the average degree of grounding

$$\overline{D}_g = \frac{1}{n_g}\sum_{i=1}^{n_g}(\gamma H_s - w_g)^2 \tag{3.20}$$

In the previous equations, if the keel depth is known or estimated, it can replace the ratio of sail height to keel depth, γ, and sail height, H_s. For a full derivation of these equations, see Druckenmiller (2011).

In order for the frictional coupling of a ridge to the sea floor to be overcome by wind or current stress, F_a or F_w ,or a combination of the two, must exceed F_{sb}. For simplicity, the stresses on the landfast ice from the wind and the current will be treated separately:

$$F_a > F_{sb} \Rightarrow L_{LFI}\rho_a c_a U_a^2 > \frac{c_f n_g \rho_w g \overline{D}_g}{\tan\alpha_k} \tag{3.21}$$

and

$$F_w > F_{sb} \Rightarrow L_{LFI}\rho_w c_w U_w^2 > \frac{c_f n_g \rho_w g \overline{D}_g}{\tan\alpha_k} \tag{3.22}$$

Using various standard values for some of the terms (ρ_a=1.3 kg/m^3, ρ_w=1027 kg/m^3, a_k=26.6°, c_f=0.5, g=9.81 m/s^2), and simplifying yields

$$1.29e^{-4} L_{LFI} c_a U_a^2 > n_g \overline{D}_g \tag{3.23}$$

$$0.102 L_{LFI} c_w U_w^2 > n_g \overline{D}_g \tag{3.24}$$

It should be noted here that currents and winds moving in the same direction will result in a larger force on the ice. The wind and the current may also oppose each other, reducing the total forcing on the landfast ice.

Besides a ridge failing at its contact with the sea floor, the ridge keel can fail if its shear strength is overcome by the destabilizing stresses. The shear strength, τ_k, of a ridge keel is given by the Mohr-Coulomb failure criterion

$$\tau_k = c + \sigma_n \tan\theta \tag{3.25}$$

where c is the cohesion strength, σ_n is the normal stress that is acting on the failure surface, and θ is the angle of friction. Croasdale *et al*. (2001) performed studies in the field to determine the cohesion strength of first year ridge keels in the Arctic, and found values of 6 to 23 kPa with an average of 14.1 kPa.

Druckenmiller (2011) also used the weight above buoyancy to describe the normal stress on a failure surface, assuming the the length of the failure surface is equal to the keel surface in contact with the sea floor (assuming unit width)

$$\sigma_n = \frac{W_g}{l_g} \tag{3.26}$$

And substituting Equations (3.15)and (3.16) into Equation (3.26)

$$\sigma_n = \frac{\rho_w g w_g (H_k - w_g)^2}{A_k \tan\alpha_k - w_g^2} \tag{3.27}$$

Thus

$$\tau_k = c + \frac{\rho_w g w_g (H_k - w_g)^2}{A_k \tan\alpha_k - w_g^2} \tan\theta \tag{3.28}$$

In all of the preceding equations, the values for ridge geometry measurements and ratios come from Timco and Burden (1997) in cases of numerical calculations. It is the shear strength of blocks in the ridge keel in contact with the sea bed or the shear strength of contact points between blocks in the keel that destabilizing forces must overcome in order for a ridge in the landfast ice cover to fail. Whether or not the ridge fails due to failure at the ice-sea floor junction or in the ridge keel ice depends on the values chosen for the coefficient of friction, c_f, for ice-sea floor failure, and the cohesion strength, c, and/or the angle of friction, θ, for ridge keel failure.

Depending on the definition of stable landfast ice, grounded ridges may or may not be holding the ice fast to the shore. Ice that is shoreward of grounded ridges cannot be a part of a breakout without the movement of grounded ridges, although ice beyond the grounded ridges may resist breaking out even under destabilizing conditions. Without actually knowing the location of grounded ridges, it is difficult to assess if the ice that breaks out is lost due to failure of the ridges, or whether another failure process has taken place.

3.2.3 Breakout events: Failure in tension

Sea ice sheets are generally assumed to fail in tension, with preexisting flaws and cracks and lower strength in tension. Tremblay and Hakakian (2006), while determining the compressive strength of sea ice from satellite imagery, estimated the tensile strength

of landfast sea ice in the Kara Sea to be about 25 kN/m^2. The tensile strength of sea ice, for wind blowing across the ice surface, is given as (Timco, 2008)

$$\sigma_t = \frac{\tau_a L_{LFI}}{\bar{z}_i} \tag{3.29}$$

where z_i is the average ice thickness. To find the tensile strength of landfast sea ice in terms of ocean current stress, simply substitute τ_w for τ_a. Assuming that there are grounded ridges in the landfast ice cover to keep ice shoreward of the ridges from failing in tension, it is only the ice seaward of the ridges that can fail. The tensile stress then becomes

$$\sigma_t = \frac{\tau_a (L_{LFI} - y)}{\bar{z}_i} \tag{3.30}$$

such that y is the length of ice from the shore to the seaward side of the grounded ridges. Therefore, if the wind or current stress acting on a length of ice beyond the grounded ridges is large enough to overcome the tensile strength of the ice, the ice will fail in tension. Changes in sea level are one method for decreasing the tensile strength of sea ice seaward of grounded ridges. By lowering the water level in which grounded ridges sit, the ice around them will drop in elevation and can lead to cracks between the ridges and surrounding ice. This flexural failure is a special case of failure in tension.

3.2.4 Changes in sea level

As has been shown, many modes of failure of the landfast ice cover can depend on changes in local sea level. Flexural failure of ice seaward of the grounded ridge zone is more likely to occur with a drop in sea level, while the grounding strength will increase with the same drop in water depth by increasing the area of the keel in contact with the sea floor. Rises in sea level can lower the grounding strength by lifting the ridge keel from its gouge. A drop in sea level followed by a rise, can reduce the grounding strength

of ridges, as the drop can shorten ridge keels (assuming the unconsolidated portion breaks and does not significantly deepen the gouge) which are then more easily lifted out of their gouge by a rise in water level.

The tidal range for the Chukchi Sea coast near Barrow is low. The National Oceanic and Atmospheric Administration (NOAA) operated a tide gauge offshore from Barrow from August 2008 to August 2010. The mean range of diurnal tides, between mean higher high water and mean lower low water, from these data was 0.20 m (Sprenke *et al*., 2011). Tidal range can also be observed from the UAF Sea Ice Group's Mass Balance Site near Barrow, although gaps in that data set make the NOAA data more useful. The Mass Balance Site data that is available agrees well with the NOAA data. Since the tidal range at Barrow is relatively low, other causes in sea level seem to be more important in causing breakout events. Non-tidal changes in sea level include storm surges, wind-driven up- and down-welling currents along the coast, and changes in atmospheric pressure.

Changes in sea level atmospheric pressure affect sea level according to the inverted barometric effect. A drop in pressure of 1 hPa will cause sea level to rise about 1 cm. The range of sea level atmospheric pressure variations near Barrow is on the order of 100 hPa at maximum (Stewart, 2008), so sea level can vary by up to roughly 1 m due to the inverted barometer effect. Horizontal gradients in atmospheric pressure also give rise to ocean currents, which can also alter the local sea level.

An upwelling wind is such that the direction in which the wind is blowing causes upwelling of sea water near the shore, effectively lowering the sea level where the upwelling is taking place. At Barrow, the dominant wind regime is from the Northeast, producing upwelling along the shore or ice edge, and dropping sea level. Conversely, a southwest wind will cause downwelling of water, and effectively raise sea level along the shore or at the ice edge. Although the dominant current direction is along the coast moving northeast, reversals of direction can be wind driven (Johnson, 1989). Weingartner *et al*. (2009) observed instances in the Alaskan Beaufort Sea in which the sea

level rose by about 1 m, then subsequently dropped by 1 m, over a period of ten days that were associated with reversals in the wind direction. Other observations from the same study showed a drop in sea level of ~2.5 m during strong upwelling wind events.

3.3 Data for breakout case studies

The Barrow Ice Observatory provided most of the data for the breakout case studies. The Observatory is an on-going program aimed at observing near-shore sea ice characteristics and dynamics, and providing useful information to the local community at Barrow (Druckenmiller *et al*., 2009). The Barrow Ice Observatory consists of a sea ice mass balance site, a land-based marine radar, a webcam, the gathering of satellite data, offshore moorings, a yearly field campaign to collect on or near-ice physical measurements, and local Iñupiat ice experts' observations. Not all of the data available through the Barrow Ice Observatory is employed in the current case studies, and will not be discussed in detail. For a full description of the Observatory's various data products, please see Druckenmiller *et al*., (2009).

3.3.1 Sea ice mass balance site

The sea ice mass balance site is made up of instruments taking measurements of various ice and meteorological conditions and posting them on the UAF Sea Ice Group's website (http://seaice.gi.alaska.edu/gi) in near real-time. Above the ice, the air temperature and humidity are measured, and snow depth is found with acoustic transducers. Within the ice, a string of thermistors provides an ice temperature profile. Below the ice are two acoustic transducers, one looking up and the other down, used in determining the thickness of the sea ice and providing information on local sea level changes. For this study, water level data from the NOAA tide gauge that was located near Barrow are used due to data gaps in the mass balance site sea level record.

3.3.2 Marine radar and webcam

A marine radar is employed in monitoring near-shore ice development and movement at a high spatial and temporal scale. The radar is a Furuno FR7112 10kW, X-band (3cm, 10GHz). The radar is situated 22.5m above sea level on one of the largest buildings in the community. The operational range of the radar is 11km, although this range varies with atmospheric conditions. The 1.65m slotted waveguide antennae provides a horizontal beamwidth of 1.2° with the vertical beamwidth at 22°. At a range of 10km, the minimum distance between reflectors must be 209m for the radar to discern them as two separate objects. At a pulse length of 0.3μm, two objects need to be approximately 45m apart in range from the radar to be resolved. With the aid of a Xenex XC2000 digital controller, the radar is operated remotely from the UAF campus in Fairbanks. The controller also captures a radar image every four minutes and archives it on a local hard drive. The archived radar imagery is sent to archiving computers in Fairbanks every 10 minutes.

Animations of the radar imagery are an excellent source of qualitative information on the development and evolution of the landfast ice cover and near-shore sea ice dynamics near Barrow. Some types of quantitative data can be extracted from the radar animations by simply observing them, examples are the amount of time the pack ice is moving to southwest or northeast, the first and last stationary ice near the coast, and the number of deformation events at the SLIE and their locations relative to the near-shore bathymetry. To generate more quantitative data from the radar imagery/animations, a program has been developed to produce gridded velocity fields by tracking mobile and stationary sea ice through consecutive radar images. The development of these programs, primarily implemented in Matlab, was a joint project between the Sea Ice Group at UAF and the Video/Image Modeling and Synthesis (VIMS) Lab at the University of Delaware (Rohith MV *et al*., 2013). After three years of joint work on this project, the programs successfully produce output relevant to geophysical sea ice research and local ice users,

and the products are to be posted on the Sea Ice Group's website on a daily to monthly basis.

The radar receives backscatter from sea ice features within its range of about 11 km, but changes depending on atmospheric and ice conditions. Ridges, the edges of ice floes, and other rough surface features not in the shadow of other such elements of the ice cover are discernible in the radar imagery. In general, areas of flat ice and calm open water do not generate enough backscatter to be detected by the radar (Mahoney *et al*., 2007b). Areas void of return signals do not necessarily imply flat ice or open water in that area. Ice topography, if sufficiently high, can occlude ice features at a greater range if sufficiently high enough. The strength of a radar signal is also dependent upon the orientation of the reflection surface to the impinging radar signal, as well as physical characteristics of the ice.

Whether or not an ice surface reflects energy back to the radar transceiver depends on the wavelength and grazing angle of the radar signal, and properties of the ice. A signal can be returned from the surface of the ice or from within the volume of ice. Skin depth is the depth to which the electromagnetic wave penetrates into the ice, and depends on the dielectric properties of the ice (Lewis *et al*., 1987). For sea ice, the dielectric properties are a function of the bulk salinity and brine inclusions, and therefore the age and temperature of the ice. First year ice, which has a higher bulk salinity than multiyear ice, has a smaller skin depth and is considered a 'high loss' material. Since most of the landfast ice in the radar imagery is first year ice, most of the backscatter signals are expected to come from the surface of the ice.

A transmitted radar signal that hits the ice surface can be reflected away from the radar or scattered in many directions. The difference depends on whether the surface is smooth or rough, according to the Rayleigh criterion (Lewis *et al.*, 1987)

$$h < \frac{\lambda}{8 \sin \Psi} \tag{3.31}$$

where h is the roughness height of the surface feature, λ is the wavelength of the radar signal, and Ψ is the local grazing angle the radar wave hits the surface. The grazing angle is relative to the orientation of the surface. For flat ice or calm water, the grazing angle will vary with distance from the radar transceiver, so the Rayleigh roughness height changes linearly with range from the antenna (Mahoney *et al*., 2007b). Specular reflection occurs from these surfaces, except for a few hundred meters range from the radar, due to the low elevation of the radar unit. Signals received from farther out than these few hundred meters will come from surfaces that satisfy Equation 3.31 or are oriented such that the local grazing angle is high enough to scatter a signal back to the transceiver.

The webcam component of the Observatory is located just under the radar unit. Images are taken every four minutes, and archived locally as well as sent to UAF where they are stored and posted on the Sea Ice Group website. The webcam is oriented in a NNW direction, and so overlooks the landfast ice or open water. The goal of the webcam is to visually document seasonal events in local sea ice regime, such as the first appearance of ice in the near-shore waters, deformation of landfast ice, breakouts, and the onset of melting and breakup.

3.3.3 Satellite products

There are many satellite data products available to the Barrow Ice Observatory via the Alaska Ocean Observing System and the Geographic Information Network of Alaska. In this study, synthetic aperture radar (SAR) imagery collected by the European Remote Sensing Satellite 2 (ERS-2) and provided by the Barrow Area Information Database (BAID) is used to identify landfast ice edges beyond the footprint of the land-based radar, and possible pack ice interactions with landfast ice.

3.3.4 Offshore moorings

Since in the 2009-2010 ice season, the Barrow Ice Observatory includes two offshore moorings deployed in collaboration with Hokkaido University in Japan (Petrich *et al.*, 2012). The moorings are equipped with an acoustic Doppler current profiler (ADCP), a temperature-conductivity probe, and an ice profiling sonar (IPS). Salinity of the water is determined from the temperature and conductivity measurements. During the 2009-2010 ice season, one mooring was located approximately 2 km offshore from the radar's location, and was directly under landfast ice or landfast ice extensions for much of the season. The other mooring was outside of the radar footprint, southwest from the radar. For the case studies, the water current in the uppermost bin (0-10m water depth) and water temperature was analyzed.

3.3.5 Local ice observations

Joe Leavitt, an Iñupiaq whaling captain from Barrow, has made daily sea ice observations since 2006 (Eicken *et al*., in press 2013). His observations provide insight into ice dynamics and conditions that can only be made by physically observing the ice, as well as providing an alternative context in which to describe and determine the stability of the landfast ice cover. Mr. Leavitt's ice expertise has developed from many years of subsistence activities on the ice, requiring him to constantly evaluate the condition of the ice, the weather, and currents in order to be successful and safe.

3.4 Methods

3.4.1 Detection of breakout events

Defining the seaward landfast ice edge (SLIE) is a difficult task, as what appears to be the edge of the ice attached to the coast can change rapidly. Previous work by Mahoney *et al.* (2005) employed a 20 day time period to define the edge of the landfast ice; if ice extending from the coast remained stationary for 20 days, it was considered

part of the landfast ice and the edge was seaward of the stationary ice. This time period was chosen based on typical synoptic time scales and the repeat interval of Radarsat SAR scenes of the Eastern Chukchi and Western Beaufort regions. In the current case studies, a time period of seven days of stationary ice was chosen to determine whether or not ice in the near-shore region is considered part of the stable landfast ice or an extension that will drift away once the conditions holding it adjacent to the true SLIE change. This much shorter time period is possible due to the much higher temporal resolution of the coastal sea ice radar over satellite imagery, and a smaller area of observation covered by the radar. Also, this shorter time reflects local use of the ice cover on shorter time scales.

The seven day definition of landfast ice is important when determining if divergence of ice seen in the radar animations corresponds to a breakout event or the drifting away of a landfast ice extension. Landfast sea ice behind grounded ridges is considered to be stable, as it is the grounded ridges that prevent the ice from becoming mobile. Without actually determining whether or not ridges are grounded, some other measures must be employed in order to determine if the landfast ice cover is stable. One way to determine whether or not the landfast ice is stably attached is that it does not drift away under conditions that would cause it to do so, such as strong easterly winds or offshore currents. Also, the longer the ice remains motionless, the more likely it is stably attached to the coast by grounded ridges.

In order to identify breakout events, radar animations for the 2008-2009 and 2009-2010 ice seasons were analyzed, as explained in more detail below. After the first appearance of stationary ice on the shores near Barrow, the length of time any portion of ice remained immobile was tracked. The boundary between visibly moving ice and stationary ice was noted on a daily basis from the radar animations. When the boundary between stationary landfast ice and moving ice or open water remained in the same position for at least seven days, and then moved closer to the shore due to loss of landfast ice, a breakout is considered to have occurred. If the radar footprint was filled with stationary ice, such that the SLIE could not be determined, then the ice became mobile,

the resulting SLIE was compared to the most recent previous SLIE to determine if a breakout occurred.

Based on the extent of landfast ice, and the amount of ice that is lost from the landfast ice cover in the breakout, an index for the severity of the breakout was developed. A breakout of Severity Level 1 occurs if less than half the landfast ice cover breaks out, gauged by distance of the SLIE from the shore, but the SLIE moves shoreward by at least 0.5 km in the area of the breakout. If the distance of the SLIE from the shore is reduced by more than 0.5 km, but remains at least 1 km from the shore, a breakout of Severity Level 2 occurred. Severity Level 3 occurs when the SLIE is reduced to less than 1 km from the shore. Since the deployment of the radar during the 2006-2007 ice season, there have been three breakouts at Severity Level 1, five at Severity Level 2, and one at Severity Level 3, for a total of nine breakouts observed with the radar.

3.4.2 Tracking sea ice in the radar imagery

The problem of tracking ice features through the radar imagery is challenging due to the characteristics of the data gathered. Visible radar return signals are typically from the surface of rough ice, such as ridges or smaller bits of ice oriented so as to reflect the radar signal. The area within the range of the radar may not be filled with ice, or appear to not be filled with ice due to occlusions that also pose a problem to traditional tracking algorithms for radars (Rohith MV *et al.,* 2013). Grouping the radar reflectors together for tracking, while possibly a valid assumption because a floe is a single object, is difficult because of occlusions and non-rigid transformations of the ice (breaking or colliding). Thus traditional feature tracking methods, and methods for choosing features for tracking, are not suitable for tracking sea ice from marine radar imagery, instead, a combination of existing and new methods are used.

Since there are areas of the radar imagery with many features that need to be tracked and areas with few, both dense and sparse optical flow tracking methods are

performed over the imagery (Rohith MV *et al.,* 2013). The dense method is used in areas where more reflectors are visible, while the sparse tracking method finds the motion field for subregions of the image. A Normalized Cross Correlation (NCC) method in 5x5 pixel windows is used to estimate the dense motion field. For the sparse field, a multiscale Harris operator is employed to identify trackable features in the radar imagery, which finds areas of the imagery with a corner like appearance. Once identified, the features are tracked through consecutive radar images with a Lucas-Kanade-Tomasi (LKT) tracker. The LKT tracker uses intensity derivatives around the tracked feature in direction and time, and assumes the velocity of a feature is the solution to a linear system of relationships between the feature's intensity derivatives across consecutive images. Occasionally in the imagery, radar reflectors can flicker, so tracked features are only accepted if they are visible in three consecutive images. Once the velocity fields for all tracked features have been generated, a dense motion field is created for the entire image by linear interpolation with the NCC field. Any velocity estimates from the LKT method that differ by an operator-chosen threshold from the velocities estimated with the NCC method are discarded. For a complete review of the sea ice feature tracking program, please see Rohith MV *et al* (2013).

3.4.3 Estimation of grounded ridge extent

With the gridded velocity fields output by the ice tracking program, an estimate of the number, and length, of grounded ridges is possible by computing deformation fields. A principal orthogonal component of the two dimensional strain field is given by (Thorndike, 1986)

$$E_I = \frac{\partial u_x}{\partial x} + \frac{\partial u_y}{\partial y} \tag{3.32}$$

where E_I is the divergence/convergence component, and u_x and u_y are the velocity components in the x and y directions respectively. Since the velocity components are regularly gridded, the derivatives in the equation above can be approximated with a centered difference scheme (Mahoney *et al*., 2004). Divergence represents a change in area, with positive values describing separation or gain of area and negative values being convergence or loss of area.

Since the velocity output of the ice tracking program is in pixels/8 min (a velocity of 1 pixel/8 minutes is approximately 0.045 m/s) for every set of three images, and the grid size for the velocity field is 10x10 pixels, a divergence of -1 would mean the area of 100 pixels is lost in convergence. In the first preprocessing step of the ice tracking program, the size of the radar image is halved in both dimensions resulting in an image that is 512x512 pixels (Rohith MV, *et al*., 2013). Therefore, each pixel that is processed in the tracking program corresponds to 2x2 pixels from the raw radar imagery, resulting in the size of one grid cell in the velocity field actually representing 400 (20x20) pixels in the radar image. The size of one pixel in the radar image has been shown to be ~21.5x21.5m. This corresponds to an area of ~184470 m^2 being lost to compressive deformation with a divergence of -1, which may represent ridging. If the parent ice thickness is 1 m, the total volume of the ridge along the edge of the 20x20 pixel velocity grid cell would be 184470 m^3. Divide this number by 20 (pixels) and the width of a pixel, to get 429 m^3 of ice in 1 m of ridge length, or an area of 429 m^2 in cross-section. Using a keel porosity of 0.3, and therefore a sail porosity of 0.22, and a ratio of keel area to sail area at 8 (Timco and Burden, 1997), the area of a cross-section of the keel would be 528 m^2 while the sail would be about 65 m^2. Using Timco and Burden's (1997) 3.9 ratio of keel width to keel depth, and assuming a triangular ridge shape, the depth of the keel would be 16.5 m.

In a case in which the ridge keel reaches the sea floor and compressive deformation continues towards the ridge, the ridge will grow seaward, and take on a trapezoidal shape. The sail can also cease to gain height and grow wider. Here it is

assumed that macroscopic porosity of the ridge does not change with the change in direction of primary ridge growth from vertically to laterally, and that the ridge keel does not significantly gouge into the sea floor. With the same parameters as the triangular ridge case, that is 1 m thick parent ice and 30% porosity, the total volume of the ridge keel will not change from 520.6 m^3, or 520.6 m^2 in cross-section 1 m in ridge length. If the depth is taken constant at 12 m in the location of the ridge formation, the width of the ridge's keel in contact with the sea floor would be ~19.4 m, and the total width of the ridge keel near the ice surface would be ~67.3 m. Using the difference in the calculated keel depth of 16.5 m and a water depth of 12 m, and using Equations 3.19 and 3.20, this grounded ridge would have a frictional coupling with the sea floor on the order of 204 kN/m.

Hypothesized ridge geometry plays an important role in estimating the strength of a grounded ridge's coupling to the sea floor. The ridge geometry used in this work is based on the ridge characteristics described by Timco and Burden (1997), who only considered floating ridges. Since the current work focuses on grounded first-year pressure ridges, ridge geometry can differ significantly from that of a generalized first-year pressure ridge that is floating. One of the characteristics of ridge geometry implicit in the equation for determining a ridge keel's coupling to the sea floor is the angle of the ridge keel, α_k.

3.5 Breakout events

There were a total of nine breakout events observed in the radar animation data between the 2006-2007 ice season and the 2009-2010 ice season (Table 2.1). The decision on which breakout events to study in depth was driven by the availability of environmental data leading up to and during the breakout event, level of severity of the breakout event, whether or not the breakout occurred during the stable period of the ice season, and relevance to the local whaling community in the context of stability of the ice cover. The breakouts chosen occurred on February 27, 2009 and March 24, 2010. Both

were of severity level 2 (see Chapter 2.4) and both took place after the seaward landfast ice edge extended into water 18-20 m deep representative of the stable period of the annual landfast ice cycle.

3.5.1 February 27, 2009 breakout: Pre-breakout ice conditions

In any description of a breakout event, it is important to review the formation and growth history of the landfast ice that is involved in the breakout and the ice that remains attached to the coast. As pointed out earlier, the marine radar provides an excellent data set for determining the development of the seasonal landfast ice near Barrow. The following is a description of relevant events preceding the February 27, 2009 breakout. The ice conditions are also compared to Leavitt's near-daily observations (Leavitt, unpubl. observations: see also Eicken *et al*., in press 2013). Table 3.1 gives the dates of important developments in the landfast ice cover before the breakout event. Note that when the radar footprint is mentioned, it is only the oceanic portion of the radar imagery that is being referenced.

The first ice seen in the radar imagery appeared on October 16, 2008, although a review of the webcam imagery showed flat ice extending from the shore the day before. This ice did not stay long, with the shore free of ice on October 17 (from webcam). Following the first appearance of ice, there were multiple instances of ice moving

Table 3.1. Dates of important events during the 2008-2009 ice season.

Event	Date
First mobile ice visible in radar imagery	October 16, 2008
First stationary ice visible in radar imagery	November 6, 2008
SLIE reaches ~20 m water depth	February 13, 2009
Emplacement of ice that breaks-out	February 19, 2009
Breakout event	February 27, 2009

northeast visible in the radar imagery, or near the coast visible in the webcam, though none of this ice became incorporated with the landfast ice that formed shortly after this period. Ice first became caught in the near-shore area on November 6, when pack ice that was drifting southwest became immobile after it converged on the coast. The seaward landfast ice edge (SLIE) at this time was ~0.5 km from shore. Leavitt's observations agreed with this finding, stating that pan ice was pushed to the shore under a north wind (Leavitt, unpubl. obs., 2008).

The next significant change in SLIE position occurred over December 19-20. Shearing and convergence at the SLIE caused the edge of the landfast ice to move seaward, such that after the mobile ice drifted away from the landfast ice, the SLIE was a little over 1 km from the shore. The ice that made up the landfast ice at this point remained until break-up at the end of the ice season in June 2009. Leavitt also observed the water was 'closed up' with some ridging having occurred 2 miles down the coast about 3/8 mile out' (Leavitt, unpubl. obs., 2008).

On February 6 the radar footprint was filled with stationary sea ice, and a SLIE could not be determined until February 10, when the ice, except for the ice shoreward of the previous 1 km SLIE, shifted seaward about 0.5 km There were obvious openings between the mobile ice and the stationary landfast ice after this slight shift, in agreement with Leavitt's observations for this day. When the ice began to move southwest on February 13, convergent deformation on the seaward side of these openings was apparent, and the SLIE moved out to about 2 km offshore. This is an important addition, as the water depth is 18-20 m about 2 km from the shore, indicating the beginning of the stable ice period according to Mahoney *et al*. (2007a). It is also important to note that this ice also survived as a part of the landfast ice until the end of the ice season. Leavitt's observations indicate it was foggy and cloudy during this period, although he saw open water ~1 mile out on February 14 (Leavitt, unpubl. obs., 2009).

On February 15, convergence of the pack ice shoreward caused what appeared to be new ice to deform at the ~2 km SLIE, possibly adding to ridges at the SLIE. On February 16, Mr. Leavitt's observations state that the ice edge was about 3 miles out, with a flat pan of ice extending from a ridge (Leavitt, unpubl. obs., 2009). This was not visible in the radar imagery, possibly due to occlusion of the radar signal by the ridge or the low topography of the extension. A similar event as the one on February 15 occurred on February 17, with convergence of new ice or the flat extension on the SLIE. This event was also accompanied by possible ridging deformation in the pack ice as it moved shoreward in the oceanic portion of the radar footprint that appeared to be filled with ice. The edge of the pack ice during this event converged all the way to the SLIE identified in the radar imagery. Therefore any new/flat ice in between would have been shoved into ridges at the SLIE or pack ice edge, assuming 100% ice cover in the converging pack.

On February 18, the SLIE was 2 km from shore. Yet again, on February 19-20, the pack ice converged on the SLIE from the West, deforming what appeared to be new ice and deformation taking place in the pack itself, and filling the radar footprint with ice. On February 21, the ice became mobile with the SLIE being ~5.5 km offshore. This was the ice that was involved in the eventual breakout event on February 27.

After the ice drifted away on February 21, there was no movement in the radar footprint until late in the day of February 23 when ice drifting to the Northeast became visible. The movement northeast continued until late on February 25, when the radar footprint became filled with immobile ice. There was no movement of radar reflectors in the oceanic portion of the radar scene until between 7:29 and 7:33 on February 27. When the breakout occurred, ice began to move almost due north, leaving the SLIE about 2 km from shore adjacent to Barrow.

3.5.2 February 27, 2009 breakout: Conditions during the breakout event

The environmental conditions during the breakout events are used to estimate the atmospheric and oceanic stresses acting on the landfast ice, as well as track other

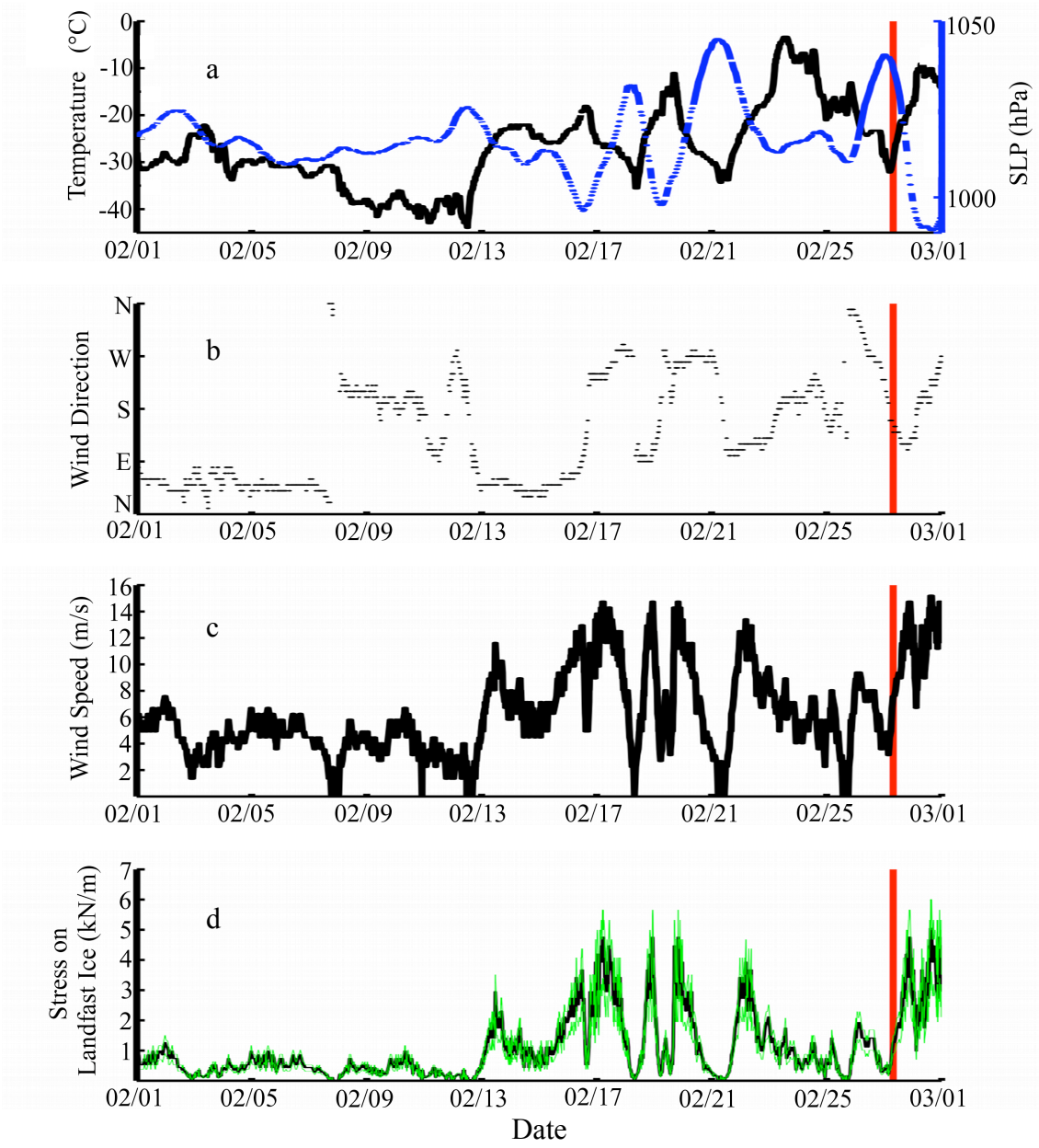

Figure 3.3. Atmospheric conditions for February 2009, and estimated stress on landfast ice. Red vertical line indicates time of breakout event. a) Air temperature and sea level pressure (blue). b) Direction the wind was coming from. c) Speed of the wind. d) Estimated stress on landfast ice from wind with the drag coefficient c_a as 0.0042 (black line), and ranging from 0.0015 to 0.008 (green lines; Guest *et al.* 1994).

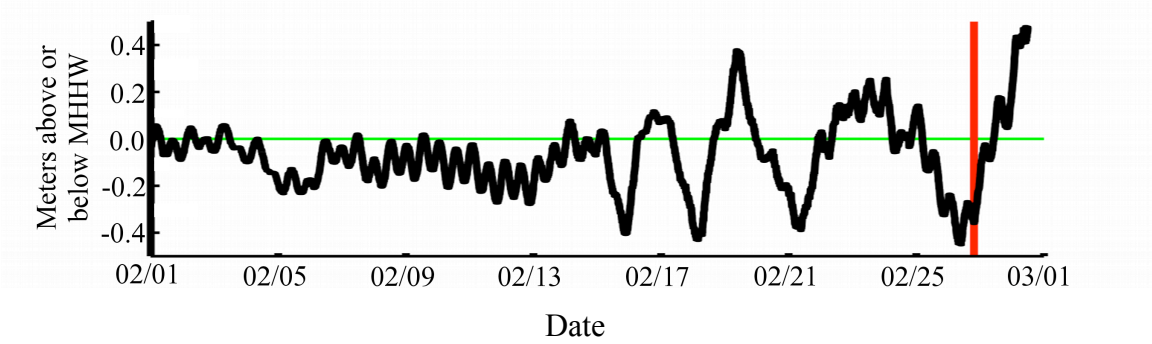

Figure 3.4. Water level for February 2009. The water level is relative to mean high higher water (MHHW; green line). Red line indicates time of breakout.

processes which may contribute to an increase or reduction in the stability of the landfast ice cover. Estimates of the degree of grounding of pressure ridges formed in-situ, based on the convergent portion of divergence calculations on the ice drift velocity fields, are also presented.

The atmospheric conditions leading up to and during the breakout event on February 27, 2009 are shown in Figure 3.3, while water level (relative to mean higher high water, MHHW) is shown in Figure 3.4. The data given are air temperature, sea level pressure, wind direction, and wind speed. The effective stress on the landfast ice was found using Equation 3.12, with ρ_a=1.3 kg/m^3, c_a=0.0042, and L_{LFI}=4 km from the radar imagery.

At the time of the breakout winds were coming from the SSE, moving nearly directly offshore at 7 m/s, for an effective stress of ~1.5 kN/m across the 4 km ice that broke-out. The sea level was rising from a short drop (relative to MHHW). It is important to note that the sea level data from the NOAA tide gauge have been corrected for atmospheric pressure and give true water depth.

With the ice that broke-out coming into place on February 19-20, the ice experienced similar wind conditions on February 25, with wind from the SSE at about

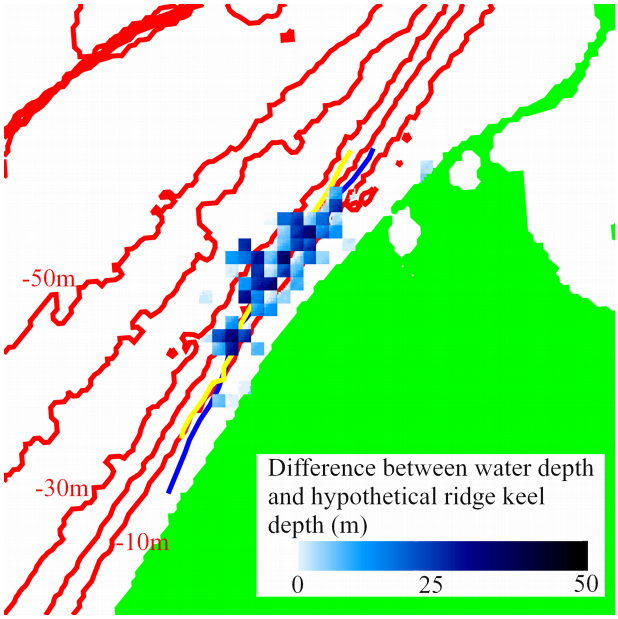

Figure 3.5. Map of possible areas of grounded ridges before February 2009 breakout. Hypothetical keel depths are estimated from divergence calculations. Darker grid cells represent more heavily grounded areas. Red lines are bathymetric contours at 10 m intervals extending from the coast (green). Blue line indicates landfast ice edge before the breakout; yellow line after the breakout.

7-8 m/s although the water level was ~0.5 m higher. On February 21-22, the wind was also offshore and much stronger, around 12-14 m/s. Water level was rising from a large drop that occurred after the deformation events on the 19th and 20th. The water level dropped to its lowest level for the whole month of February on the 26th. Despite offshore atmospheric stresses of the same magnitude or more acting on the ice that broke-out, the landfast ice did not breakout.

An estimation of the extent of grounded ridges is given in Figure 3.5. In order to estimate the degree of grounding, the parent ice sheet thickness used in the calculations is 0.95 m, from the mass balance site. The calculated divergence fields from the sea ice velocity fields were summed from the time period of February 17 to the time of the breakout on February 24. Only the negative divergence values were retained, representing the convergence of sea ice in the radar imagery. Positive divergence values may not reflect actual divergence in the sea ice cover due to the nature of the radar imagery. Bathymetry for the Barrow region is provided by NOAA. The gray scale grid cells in the offshore portion of the image represent the difference between estimated keel depth and water depth, with darker cells being more extensively grounded than lighter grid cells. The number of heavily grounded grid cells and the difference between average

water depth for that grid cell and keel depth are used in the calculation of the degree of grounding of the landfast ice that ultimately broke-out. In this case, there were 32 heavily grounded grid cells, providing a grounding strength on the order of 70000 kN from ridge keel-sea floor coupling.

3.5.3 February 27, 2009 breakout: Discussion

The following section describes any conditions that may have contributed to, or detracted from, pre-conditioning the landfast ice for a breakout event to occur. Possible modes of failure of the ice extent or grounded ridges are also discussed, and stresses that could play a part in the breakout event occurring.

Based on Equation 3.23, the wind stress of ~1.5 kN/m acting on the ice would not have been sufficient to overcome the estimated grounding strength, unless the shorefast ice was wider than ~48 km. While the ice that broke away was wider than the footprint of the radar, the extent of landfast ice in this area of the Chukchi Sea is not likely to extend as far as 30 to 40 km offshore (Mahoney *et al.*, 2007a). If the ice that broke away would have been wide enough, then at the same time the grounding strength may have been increased due to grounded ridges formed outside the footprint of the radar farther away from the coast. However, since the water depth increases, it is unlikely that many other ridges would have become grounded. Assuming the landfast ice that broke away was less than 48 km wide and the only grounding of pressure ridges occurred in the radar footprint, then it appears that the ice that broke out on February 27, 2009 was pre-conditioned for the breakout. If the divergence calculations are valid for the deformation events that took place on February 19th and 20th, and grounded ridges resulted, these features would have provided anchoring strength to the landfast ice cover. On February 21, the ice cover experienced offshore stress that was stronger than the offshore wind stress during the breakout event. While there were offshore winds on the 21st, sea level was dropping to a lower level than any the ice had experienced up to that point. This would result in an increase in the grounding area of the ridge, provided the strength of the

contact points between blocks within the unconsolidated portion of the ridge near the sea floor was overcome, and compaction of the ridge keel would then have taken place. However compaction of the ridge keels may not have taken place with this drop in sea level, because the offshore stresses persisted up to February 23 while the water level was rising, and could have lifted any shortened keels off of the sea floor. If the ridge keels had been shortened by the drop in sea level, the offshore wind could have pushed the ice away unless there was other resistance to the offshore stresses. The drop in sea level on February 21 may not have caused flexural failure of the ice seaward of the post-breakout pressure ridge line, and thus the offshore stress may not have been large enough to overcome tensile strength of the landfast ice at this junction. Alternatively, the ridge keels may not have been compromised, and remained grounded after the rise in sea level. Without ocean current data available for 2008/09, it is not known what role currents could have played in the breakout.

Shortly before the breakout event, on February 26th, the water level dropped to the lowest level of that month. This may have caused shortening, or have further shortened ridge keels, and the subsequent rise in sea level would have lifted shortened keels off the sea floor. With the wind from the North on the 25th swinging around to come from the South on the 27th, the effective wind stress on the ice would have been shoreward until the wind had nearly completed this change. When the ice did breakout, it moved away to the North, following the wind. The sea level drop, in this instance as well, could have resulted in a flexural failure at the tide crack, if refrozen, between the landfast ice seaward of the remaining post-breakout ridge line. In another possible scenario, the tensile strength at this junction was overcome by the wind forcing.

This outcome is somewhat speculative without ocean current observations. For instance, onshore currents could have been opposing the offshore winds on February 21, holding the landfast ice in place. Then on February 27, the currents could have been offshore, or not strong enough to fully oppose the wind stress on the ice, contributing to or allowing the breakout to take place. Also, due to the nature of the radar imagery, the

thickness of the ice that contributed to ridge building is not known. Here it is assumed to be level ice of the same thickness as ice that grew at the mass balance site, which is northeast of where the ridge building occurred. The ice involved in the ridge building process is most likely thinner than that at the mass balance site.

3.5.4 March 24, 2010 breakout: Pre-breakout ice conditions

Table 3.2 gives the dates of important events in the 2009-2010 ice season. The first visible drift ice in the radar imagery appeared on November 4, 2009, moving southwest. There may have been ice drifting through the radar footprint prior, but before October 25 we lack continuous radar coverage. On November 13, pack ice was drifting to the Southwest and converging on the coast such that individual floes appeared to get stuck near the shore. The following day, a reversal of drift direction caused ice to converge along the shore for the entire length of the coast in the effective radar footprint. Leavitt (unpubl. obs., 2009) observed that ice piled up close to shore along the coast at that time. Some of this ice was stationary while ice more seaward was still moving. Late on November 16 and into November 17, the ice in the radar imagery became stationary. Slight movements of radar reflectors greater than 1 km from shore over the next two days showed that ice within about 1 km of the shore may have been the beginning of the

Table 3.2. Dates of important events during the 2009-2010 ice season.

Event	Date
First mobile ice visible in radar imagery	November 4, 2009
First stationary ice visible in radar imagery	November 13, 2009
SLIE reaches ~20 m water depth	March 3, 2010
Emplacement of ice that breaks-out	March 17, 2010
Breakout event	March 24, 2010

landfast ice cover. On November 20, the ice began to move north, leaving ~1 km of ice on the shore. Leavitt stated that stationary ice extended to 'about 1000 yards out from beach (Leavitt, unpubl. obs., 2009). This ice remained immobile for the remainder of the 2009-2010 ice season, which ended in mid-June. Leavitt did not make observations between November 24, 2009 and January 5, 2010.

On March 2, ice became mobile that had been stationary in the radar imagery since February 27. It is unclear whether or not the entire radar footprint was covered with ice because large areas lack radar reflectors during that time. Leavitt's observations indicate these areas were covered with young ice (Leavitt, unpubl. obs., 2010). Once the ice began to drift to the Southwest, the SLIE advanced by about 1 km to about 2 km distance from shore. Further convergence of mobile ice onto the SLIE on March 3 pushed the edge of the landfast ice slightly shoreward with deformation occurring along the SLIE. On March 3, Leavitt noted an add-on of about 1000 feet to the landfast ice width, with about 100 feet left the next day on March 4 (Leavitt, unpubl. obs., 2010). The term add-on refers to ice that is added to the landfast ice extent, although it may not meet the immobility criteria of seven days to be considered a part of the stationary landfast ice.

On March 8, the radar footprint became filled with stationary ice. On March 9, 10, and 11 small shoreward shifts of the ice probably resulted in deformation of ice at various distances from the shore. There was no radar data for the entire day of March 13, though a comparison of final image from March 12 with the first image from March 14 showed no change in the ice cover. The ice remained stationary until March 16, when the ice moved to the North leaving the landfast ice extending 1.5 km from the shore, in agreement with Leavitt's notes. The ice continued to drift slowly offshore to the North until the morning of March 17 when it began to take a more easterly drift direction. While the ice was drifting shoreward, new ice between the mobile pack ice and the SLIE was apparently being deformed. Throughout the 17th and early on the 18th, intermittent shoreward movement resulted in ridging deformation of the ice at various distances from

the SLIE, assuming 100% ice cover in the radar footprint. By ~6:00 on March 18, no movement occurred shoreward of 6.5 km from the coast. On March 19, the SLIE was left at ~6.5 km when ice more seaward drifted north/northwest. The ice that came to rest on March 17 and 18, contributing to the 6.5 km extent of the landfast ice, was the ice involved in the breakout on March 24. After the mobile ice drifted away on March 19, no movement was visible until March 22, when ice was visible moving to the Southwest beyond the SLIE. These are the same observations that Mr. Leavitt made from the shore (Leavitt, unpubl. obs., 2010). On March 24, between 12:06 and 12:22 local time, the stationary ice that had been present since March 17 began to drift southwest, breaking into 4 or 5 large pieces. The SLIE adjacent to Barrow was moved shoreward to its previous position ~1.5 km distant from shore, increasing to about 3 km from the shore farther to the North.

3.5.5 March 24, 2010 breakout: Conditions during the breakout event

The atmospheric conditions for the month of March 2010 are displayed in Figure 3.6, while water level data are shown in Figure 3.7. Current direction and velocity, and water temperature, are displayed in Figure 3.8. Principal component analysis was performed on the current direction and magnitude, and the displayed data are the two orthogonal components that explain the most variance in the data. For the alongshore data, which was the highest ranking principal component, positive values indicate currents moving to the Southwest, while negative values are currents toward the Northeast. Positive values in the onshore/offshore data are offshore currents, and negative values are onshore currents. The effective stress calculations from both the winds and the currents are also displayed in Figures 3.6 and 3.8, respectively. These were calculated with Equations 3.12 and 3.13, with ρ_a=1.3 kg/m^3 and c_a=0.0042 in Equation 3.12, ρ_w=1027 and kg/m^3, c_a=0.0175, and L_{LFI}=23 km from the radar and satellite imagery.

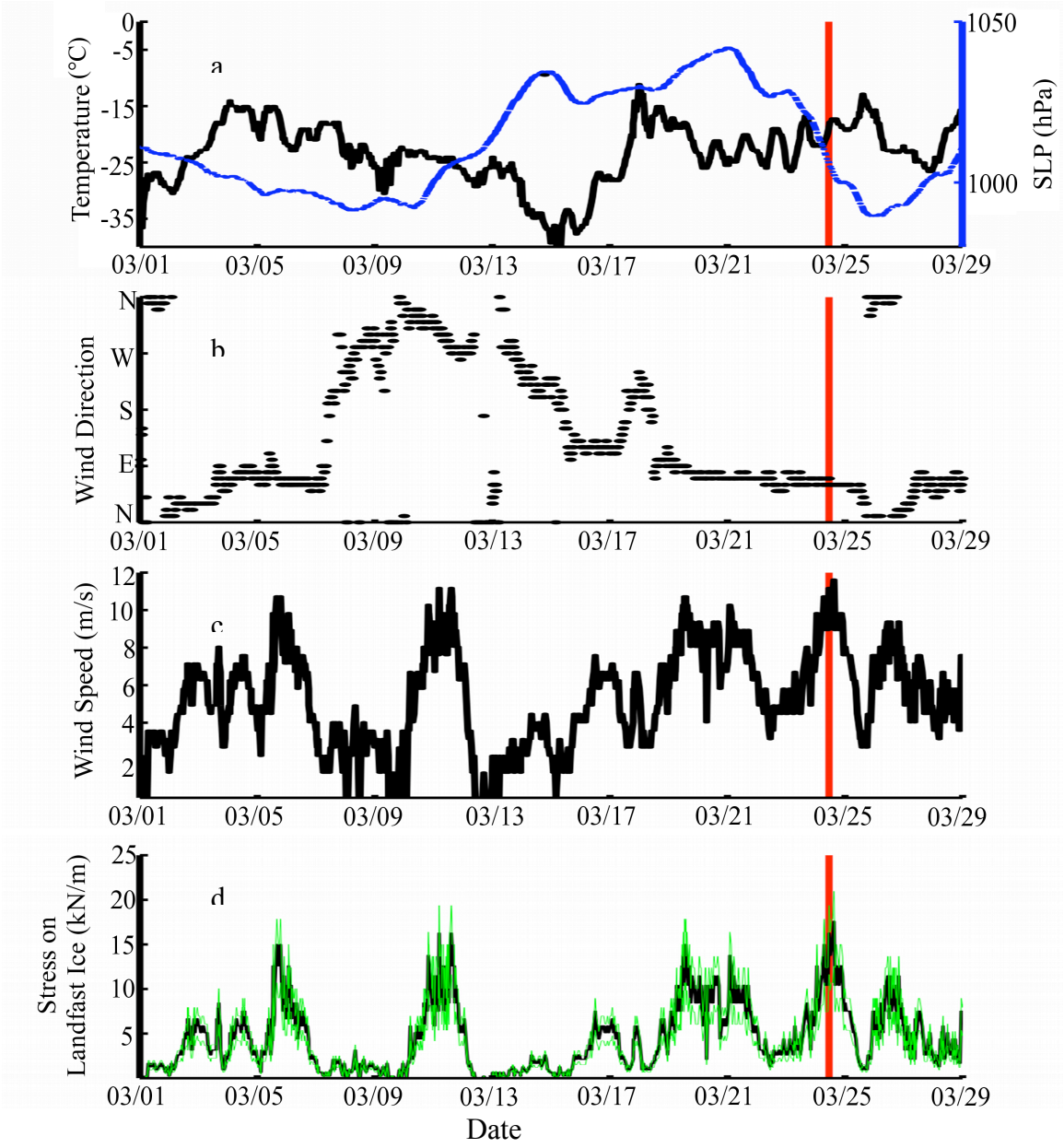

Figure 3.6. Atmospheric conditions for March 2010, and estimated stress on landfast ice. Red vertical line indicates time of breakout event. a) Air temperature and sea level pressure (blue). b) Direction the wind was coming from. c) Speed of the wind. d) Estimated stress on landfast ice from wind with the drag coefficient c_a as 0.0042 (black line), and ranging from 0.0015 to 0.008 (green lines; Guest *et al.* 1994).

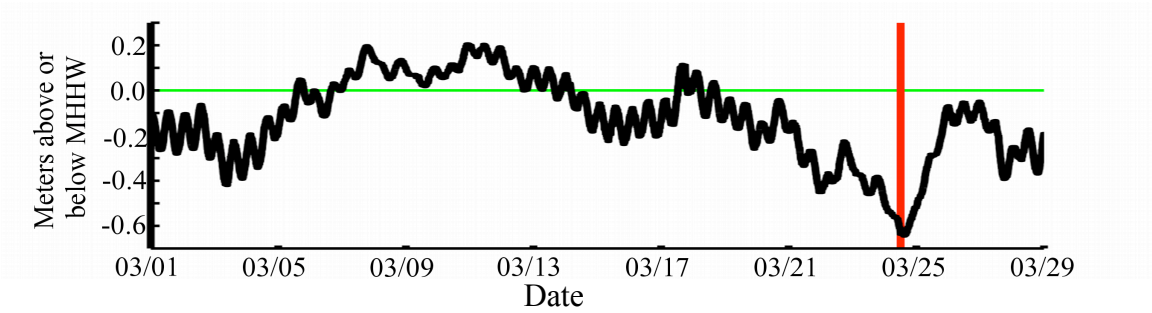

Figure 3.7. Water level for March 2010. The water level is relative to mean high higher water (MHHW; green line). Red line indicates time of breakout.

At the time of the breakout, winds were coming from the Northeast, and had been doing so for about the entire week before the breakout. The magnitude of the wind at the time of the breakout was ~11 m/s, for an effective stress of ~15 kN/m on the 23 km of ice that broke-out. The water level was dropping to a month long low, although the breakout occurred shortly before the minimum. Water temperature was slightly below -1.5°C, although it increased to ~0.5°C immediately after the breakout occurred. Water currents were to the Southwest and slightly offshore at the time of the breakout. The currents moving to the Southwest imparted an effective stress of ~60 kN/m. An estimation of the extent of grounded ridges in the ice that broke-out is displayed in Figure 3.9. The same procedure for calculating the grounded ridge estimate in Figure 3.5 is used, although the parent ice sheet thickness is 1.1 m. The summed divergence calculation ranges from March 17 to the time of the breakout on March 24. There are 31 grid cells in the ice that broke-out that are heavily grounded, providing a grounding strength on the order of ~70000 kN from ice ridge keel coupling with the sea floor.

3.5.6 March 24, 2010 breakout: Discussion

The landfast ice that broke-out on March 24, 2010 does not appear to have been preconditioned for the breakout based on the environmental data. The water level was dropping to a month-long low leading up to the breakout, and kept falling after the

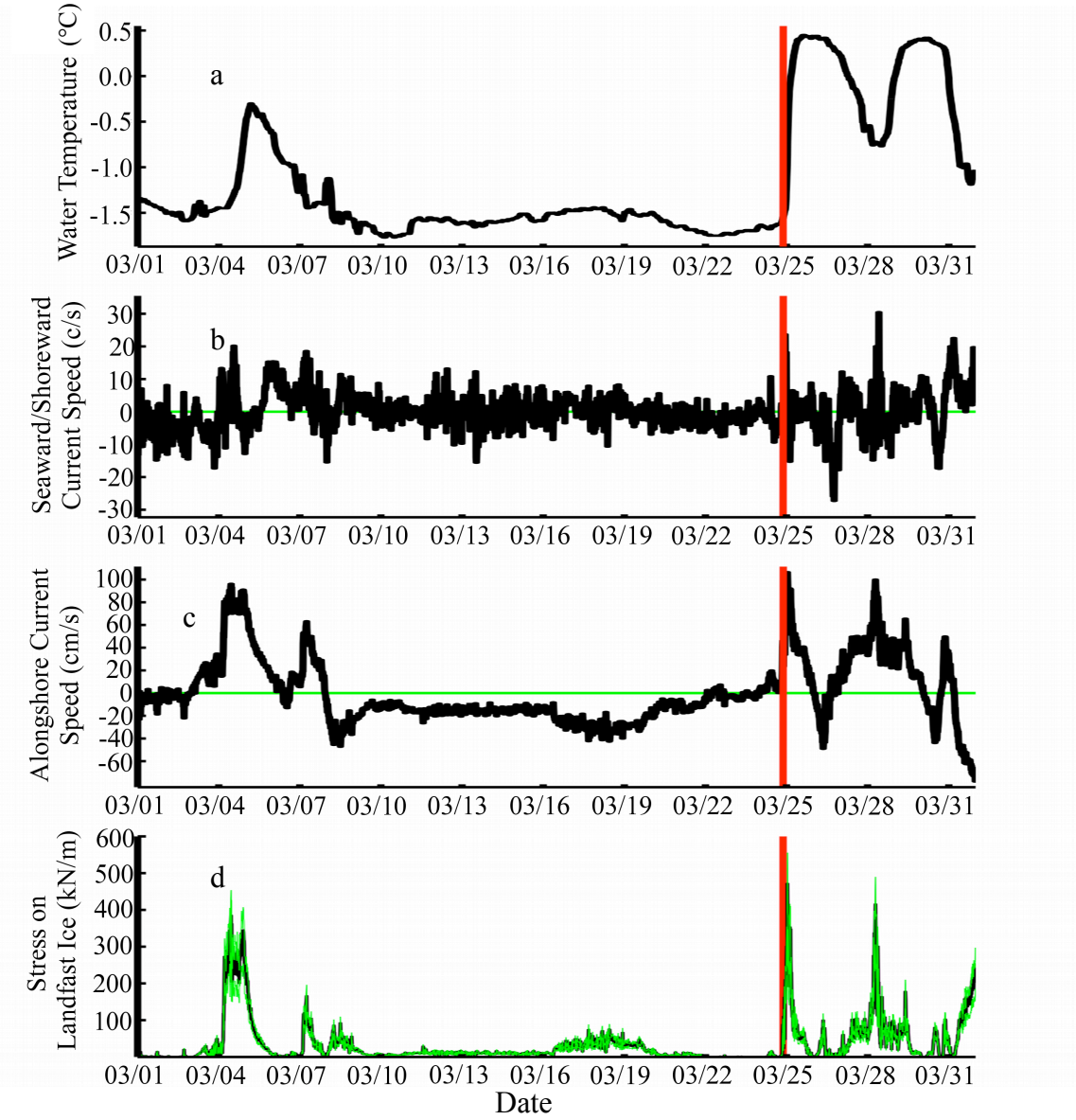

Figure 3.8. Oceanographic conditions for March 2010 and estimated stress on landfast ice. a) Water temperature measured at the Mass Balance Site. b) Seaward/ Shoreward current velocity (positive is onshore). c) Alongshore current velocity (positive is to the Northeast). d) Estimated stress on landfast ice with drag coefficient, c_w, as 0.0175 (blackline), and ranging from 0.00780 to 0.0200 (green lines; Reynolds *et al*., 1985; McPhee 1979).

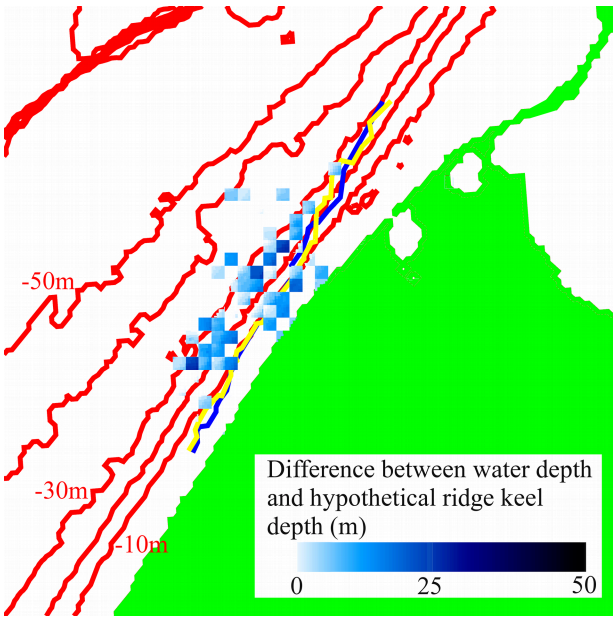

Figure 3.9. Map of possible areas of grounded ridges before March 2010 breakout. Hypothetical keel depths are estimated from divergence calculations. Darker grid cells represent more heavily grounded areas. Red lines are bathymetric contours at 10 m intervals extending from the coast (green). Blue line indicates landfast ice edge before the breakout; yellow line after the breakout.

breakout. This would indicate that shortening of the ridge keels and subsequent lifting off the sea floor could not have been a factor. Since the sea level was dropping up until the time of the breakout, the anchoring strength would have been increasing. This also means that the flexural and tensile strength of the ice beyond the post breakout ice edge could be compromised. Based on the grounding strength estimation of ~70000 kN, the combined wind and current stresses, ~75 kN/m was enough to overcome the grounding strength of the ice cover.

The winds were coming from the East/Northeast for nearly the entire week before the breakout at various magnitudes, although peaking at the time of the breakout. The currents under the ice involved in the breakout were to the Northeast nearly the entire week before the breakout, except for two short periods of relatively weak southwest currents. Shortly before the breakout, the currents reversed to be moving to the Southwest and were gaining strength such that the ice that broke-out experienced the strongest current forcing to the Southwest at the time of the breakout. Water temperature also increased slightly before the breakout, and continued to do so afterwards, which may have resulted in weakening of frozen block contacts in the ridge keel despite increasing grounding strength.

In an alternative scenario, assuming the increasing grounding strength due to sea level drop was enough to resist the wind and current stresses, rapidly moving pack ice may have come into contact with a prominent landfast ice feature, knocking the ice loose. Figures 3.10 a and b display satellite imagery, obtained by the European Remote Sensing Satellite (ERS-2), from before and after the breakout, on March 22 and March 25 respectively. The red line indicates the landfast ice edge on each day, determined from the SAR images themselves. If such an impact occurred, evidence is not visible in the radar imagery. Also, the piece of drift ice that may have knocked the landfast ice loose is not visible in Figure 3.10b.

In either scenario, once the ridges formed in the ice that broke-out, the ridges remained stationary until the breakout event. Had there been an on-shore force to move the in-situ formed ridges shoreward somewhat, the grounded ridge keels would have gouged into the sea floor. There is evidence from the radar animations that the ridges comprising the ice that resisted the breakout stresses may have been pushed shoreward in places before the breakout. Due to the nature of the radar animations and resolution of

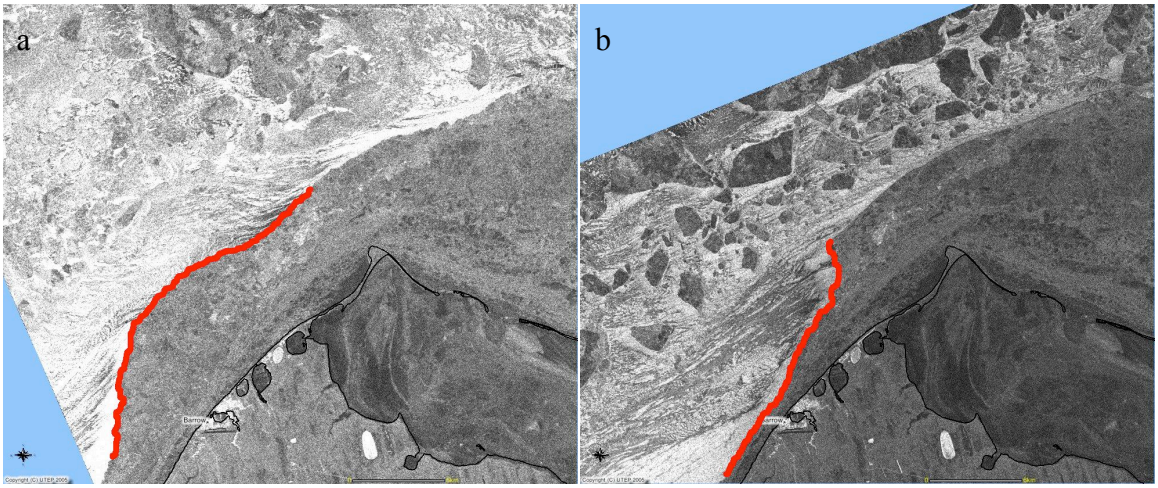

Figures 3.10 a and b. Synthetic aperture radar images captured by ERS-2 from before the March 24, 2010 breakout, on March 22 (a) and March 25 (b). The red line indicates the SLIE at the time the radar image was taken, and was determined from the satellite imagery. Ice drift was to the Southwest.

the ice velocity fields (and thus deformation fields), it is difficult to determine these ridges moved shoreward or deformation of ice was taking place in these regions.

3.6 Discussion of errors

Sources of error in the current work can arise due to a number of things, such as assumptions made about grounded ridge geometry or the spatial detail resolved by the ice tracking algorithm. The following section is a discussion of the key sources of error and how these errors could affect the conclusions concerning the cause of the breakout events under investigation.

The ridge geometry used in this study is based on the findings of Timco and Burden (1997) who characterized the shape of first-year ridges all of which were floating. While the results of that study provide a good baseline for first-year ridge characteristics, grounded ridges are the focus of this work and so may have drastically different shape characteristics. We are unaware of any in-depth study of the shape of grounded ridges performed to date.

One characteristic of a grounded ridge, for instance, that may differ from the findings of Timco and Burden (1997) is the angle of the ridge keel, α_k. A value of 26.6° was found in the previous study to be the average ridge keel angle. For ridges that form in coastal waters and become grounded, this angle may be much steeper. Since the angle of the keel dictates the depth which that keel will reach for a given volume of ice making up the keel, the grounding strength of the keel will be affected. Figure 3.11 displays the strength of the frictional coupling of the hypothetical ridge keels, formed before the February 2009 breakout, with the sea floor. The strength of coupling decreases rapidly with increasing steepness of the ridge keel angle. However, this calculation assumes that the geometry of the ridge sail scales with that of the keel, which may not hold true for grounded keels.

Directly related to the ridge keel geometry is the porosity of the ridge keel. In this study, we assumed a porosity of 0.3, also taken from the Timco and Burden (1997) study.

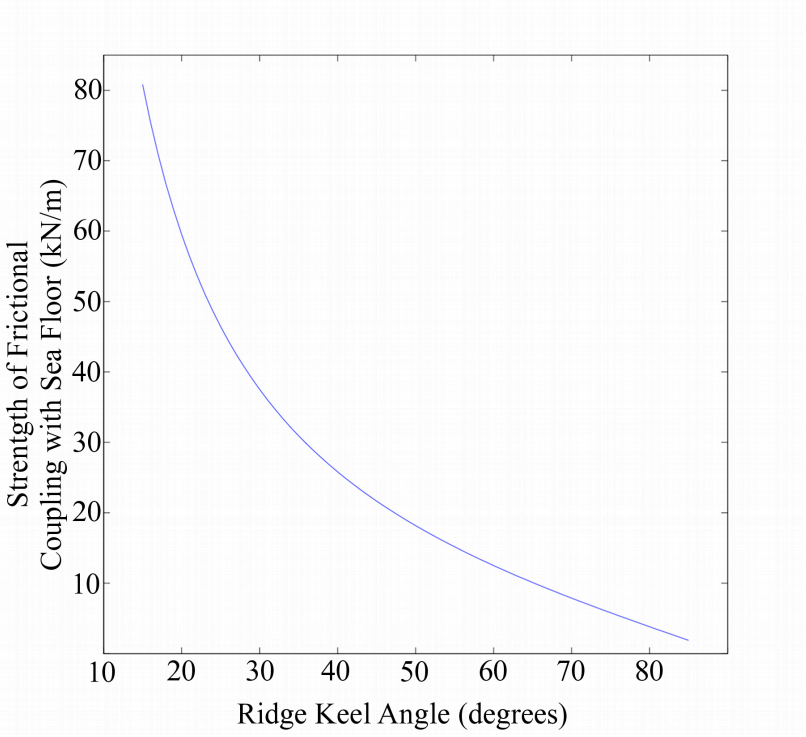

Figure 3.11. Change in strength of frictional coupling of ridge keel with the sea floor as the angle of the triangular ridge keel with the horizontal changes.

Figure 3.12 relates keel depth to porosity of the ridge keel for a single hypothetical keel with parent ice of 1m thick and from a divergence of 1. It is shown that keel depth increases as porosity increases, thus a higher number of ridge keels may become grounded assuming a higher ridge keel porosity. Traditional methods for determining keel porosity have been shown to underestimate the water content within the ridge keel volume, and new methods using nuclear magnetic resonance showed that the range of keel porosities in first year sea ice ridges range between ~0.23 to ~0.50 near Barrow, Alaska (Nuber *et al.,* 2013).

Another possible source of error in this study that affects the in-situ grounding of sea ice ridges is the thickness of the parent sheet of ice. Here, we assume that the ice that contributes to ridge building is level and of the same thickness as ice that formed quiescently at the Mass Balance Site near Point Barrow. Due to the nature of the radar imagery, the thickness of the ice involved in the ridge building process is not known, although we can assume that it is already deformed as suggested by the radar backscatter signatures. In order to determine the effects of ice thickness on grounding strength of the landfast ice cover, the ridge building calculations were carried out across a range of ice thicknesses. Figures 3.13 and 3.14 display the results of these calculations. In both

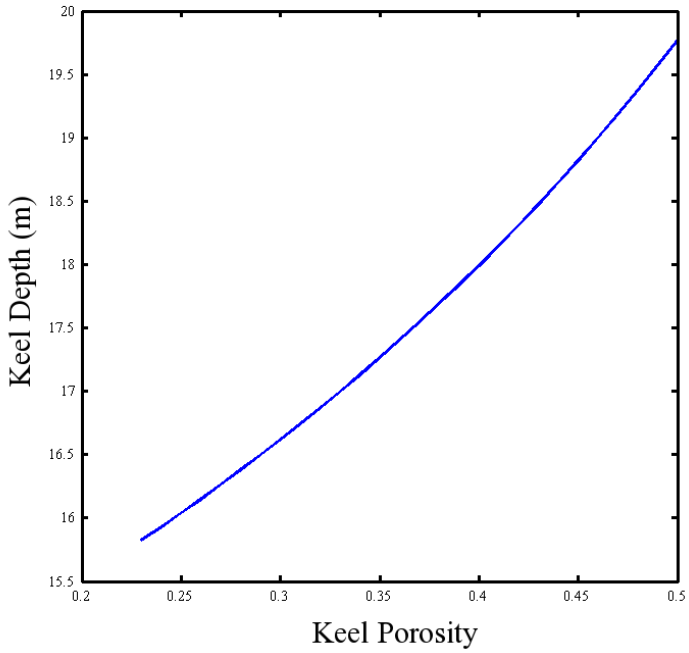

Figure 3.12. Plot of keel depths reached at different ridge keel porosities. Ridge keel depth is estimated assuming 1 m thick parent ice sheet, triangular ridge keel, and divergence of -1.

instances, the grounding strength increases with increasing ice thickness. It is interesting to note that there would not have been any hypothetical ridge keels that became grounded before the March 2010 breakout unless the ice is assumed to be at least 0.6m thick. To address the issue of unknown ice thickness on the grounding strength of the ice cover, only those deformation cells with hypothetical ridge keels that would be grounded in any part of the underlying bathymetry (the entire deformation cell is blue in Figures 3.5 and 3.9) were counted in the calculation of the degree of grounding (Eq. 3.20) and the average difference between the water depth and hypothetical ridge keel depth for that cell.

A possible large source of error arises from tracking sea ice through the radar imagery. The average error in tracking sea ice is 1.77 pixels per eight minutes (Rohith MV *et al*., 2013). This corresponds to a velocity of 0.079 m/s. Following the same procedure as in Section 3.4.3 to determine a hypothetical keel depth along with this velocity error, the range of keel depths are 15.8 m to 17.1 m. The range of frictional coupling of this ridge in 12 m of water would then be ~145 kN/m to ~261 kN/m. Therefore the velocity error associated with ice tracking could greatly increase or decrease the estimated grounding strength of the landfast ice cover. Since the deformation cells are much larger than the bathymetry resolution, it is not known where

in the deformation cell a ridge would ground, and thus difficult to estimate the influence of the ice velocity error on the estimation of grounding strength calculations. It is expected though that the velocity errors would be smaller since the area over which the velocity is being sampled is larger than the displacement of radar returns, and since the ice deformation is integrated over hours instead of just eight minutes.

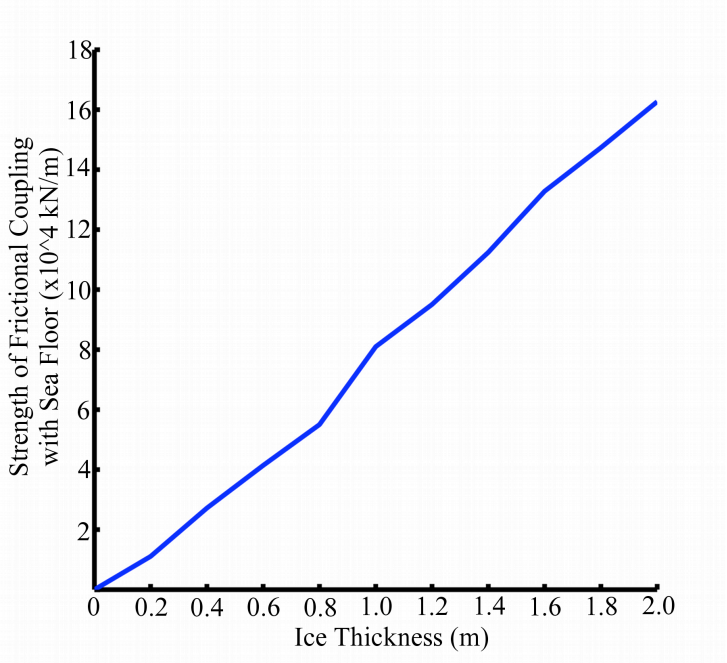

Figure 3.13. Plot of grounding strength of the landfast ice cover over a range of ice thicknesses for the pressure ridges involved in the February 2009 breakout.

3.7 Conclusions

The goal of this study was to identify the process(es) by which landfast sea ice near Barrow, Alaska could undergo a breakout event, or sudden drifting away of seemingly stable landfast ice. Two breakout events were chosen for in-depth analysis based on availability of environmental and ice property data, and relevance to the local subsistence community. Data from various sources, primarily components of the Barrow Sea Ice Observatory, were used to estimate stresses on the landfast sea ice and observe changes in conditions that worked to increase or decrease the landfast ice covers stability. Possible causes and contributing factors leading up to the breakouts were identified, although ultimate causes of the breakouts require further work.

The stability of the landfast sea ice involved in the breakouts is determined by in-situ deformation resulting in the formation of grounded pressure ridges. The extent of

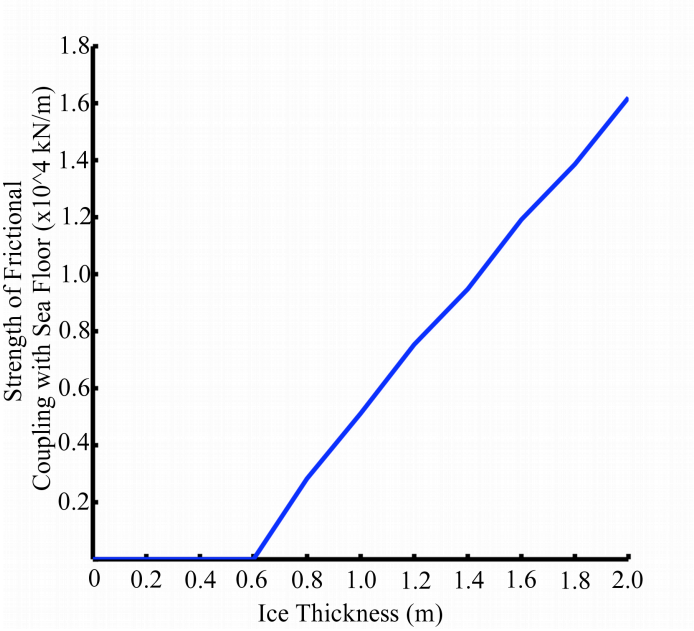

Figure 3.14. Plot of grounding strength of the landfast ice cover over a range of ice thicknesses for the pressure ridges involved in the March 2010 breakout.

grounded ridges in the landfast ice cover is estimated from the deformation field calculated from ice velocity fields produced from land-based radar imagery. It is the strength of the coupling between the grounded ridges and the sea floor that is assumed to prevent the landfast ice from drifting away under breakout favorable conditions.

Sea level changes resulting in shortening of the grounded ridge keels preconditioned the landfast sea ice for the February 27, 2009 breakout event. The landfast ice experienced stronger breakout conditions a few days earlier than the breakout occurred, but remained in place. The sea level drop the ice experienced seemed to be enough to cause non-recoverable compaction of the grounded ridge keels, priming the ice to be pushed away from the near-shore area once sea level raised and breakout conditions existed. However, without ocean current observations, this conclusion cannot be fully accepted.

Dropping sea level during the March 24, 2010 breakout would have been acting to strengthen the landfast ice by increasing the area of grounded ridge keels; there was no lifting of the keels from contact with the sea floor. The wind stress on the landfast ice cover was nearing a local peak at the time of the breakout, although the landfast ice experienced similar atmospheric conditions only a few days before on March 21, and did not breakout. The ocean currents were moving northeast on March 21, opposing the wind stress on the landfast ice. On the day of the breakout, the currents reversed

direction to follow the wind, moving to the Southwest. The combination of wind and current stress acting on the ice in the same direction was high enough to overcome the estimated grounding strength of the landfast ice that broke-out. Another cause cannot be ruled out although; interaction with rapidly drifting pack ice outside the view of the radar may have occurred, knocking the landfast ice loose.

The case studies to determine ultimate causes of breakout events near Barrow, Alaska highlight areas of research where more work is needed. The estimated grounding of ridge keels will be improved with better understanding of the macroscopic porosity of the ridge. The number and strength of contact points between ice blocks making up the unconsolidated portion of the ridge keels is another property of grounded ridges that warrants further investigation to better determine the grounding strength of grounded keels within an ice cover and the effects of dramatic sea level drops on the depth these keels reach. Considering the atmospheric and oceanic stresses acting on the landfast ice, direction dependent form drag based on surface and under ice relief would improve estimation of the force balance for the landfast ice cover.

The spatial resolution of the sea ice velocity fields could also be increased, but due to the amount of time and computing power this was not performed at the highest possible resolution for this study. An increase in spatial resolution of the ice velocity fields would help better determine areas of actual ridge grounding, and whether or not changes in radar returns around ridges at the SLIE are convergent deformation of ice or shoreward movement of the ridges. Improvements on land-based radar detection of near-shore sea ice features could refine the whole sea ice tracking program as well.

Chapter 4
Landfast sea ice breakout events:
General conclusions

Breakout events near Barrow, Alaska are typically complicated events that occur periodically during the stable period of the landfast ice season. No one single cause was identified as the ultimate driver of the breakout events considered here. Breakouts can be the product of atmospheric and/or oceanic stresses acting upon the ice to overcome stabilizing features within the landfast ice cover. The ice can be primed for the breakout through weakening of stabilizing features, via shortening and subsequent raising of grounded ridge keels, and thermal erosion of grounded ridge keels with the intrusion of warm water. In other cases, the ultimate cause for a breakout event may only be interaction with mobile pack ice knocking the ice loose. A combination of these events may also take place. Further observations of the development of a landfast ice cover and breakout events at high temporal resolution and relevant spatial scales in conjunction with atmospheric and oceanic conditions will help identify settings in which breakouts are more or less likely to occur.

Under the framework of an Arctic Observing Network, the Barrow Sea Ice Observatory is a good example of a network of data collection that provides useful information to sea ice system stakeholders (local hunters in this case) while supplying data for scientific research such as the current work and other, ongoing projects. The combination of high resolution coastal sea ice dynamic observations and the observations of an Iñupiaq ice expert aids in determining what features and processes are important to study from the perspective of the landfast ice as a platform for various activities. While gathering near-real time oceanic data such as current velocity and direction remains to be a challenge, the assessment of other near-real time environmental conditions can help determine whether or not the ice is pre-conditioned for a breakout event and raise a signal that conditions should be monitored for situations conducive to a breakout event.

Satellite data may not be available that would allow for breakouts to be observed in near-real time, though evaluation of the extent and shape of the landfast ice edge provides information on the ice's susceptibility to interaction with mobile pack ice that could result in a breakout.

While other coastal areas of the Arctic may experience quite similar or vastly different landfast ice dynamics, the processes studied in this work contributing to breakout events are applicable in other areas as well. The development of observation networks in other arctic coastal areas will encourage the comparison of different landfast ice regimes and importance of breakout-relevent processes at different locations. Coordinated field work near Barrow, as well as at other locations, will better constrain the ice cover and ridge characteristics lending themselves to the stability of the landfast ice cover. Further work on assessing the stability of a landfast ice cover and factors contributing to breakout events will help to better understand the near-shore landfast ice region as it is changing with a changing arctic, and ultimately provide useful information to stakeholder groups and decision makers in the context of rapidly changing northern regions.

List of Symbols

Symbols are listed in the order they appear in the equations throughout the text. Units, if applicable, are given in parentheses, as well as values for a specific constant.

$Dist$	distance between a SLP data value and the corresponding value at a SOM node
n	number of columns in the data matrix, or number of SLP values in the SLP distributions (931)
x_i	SLP data value at grid cell i, or SLP data value in column i in data matrix
w_i	value of the weight vector (node) in column i
t	timestep count
w	weight vector at each node in the SOM, function of t
α	learning rate of the SOM algorithm, function of t
h_{ci}	update neighborhood kernal around BMU, c, for column/gridcell i
d	distance between nodes (SOM map units)
σ	neighborhood of update
σ_0	initial size of the update neighborhood
λ	maximum number of timesteps in the training of the SOM
α	learning rate (s)
α_0	initial learning rate (s)
m	mass per unit area of ice (kg)
$\mathbf{u}$	ice velocity in the x_1 direction (m/s)
D/Dt	total derivative ($\partial/\partial t+\mathbf{u}\cdot\nabla$)
f_c	Coriolis paramter (s^{-1})
$\mathbf{k}$	unit normal vector in the x_3 direction
τ_a	air stress on the ice from wind (Pa)
τ_w	water stress on the ice from ocean currents (Pa)
g	gravitational acceleration (9.8 m s^{-2})
H	dynamic sea surface height (m)

σ_{ij} internal deviatoric stresses (Pa)

Ω angular velocity of the Earth (7.292×10^{-5} s^{-1})

ϑ latitude

ρ_{ice} density of sea ice (kg m^{-3})

z_i ice thickness (m)

c'_a ice-air drag constant (Pa m^{-1})

c'_w ice-water drag constant (Pa m^{-1})

U_a wind velocity (m s^{-1})

U_w current velocity (m s^{-1})

ρ_a air density (1.3 kg m^{-3})

ρ_w water density (1027 kg m^{-3})

c_a ice-air drag coefficient

c_w ice-water drag coefficient

c_{10} skin drag coefficient

c_f form drag coefficient

$\overline{h}_s$ mean ridge sail height (m)

N average number of ridges in the downwind direction (m^{-1})

F_a force imparted on ice from winds (N)

L_{LFI} extent of landfast ice

F_w force imparted on ice from water currents (N)

σ_{sb} shear stress at sea floor from frictional coupling (Pa)

W_g weight of a grounded ridge with buoyancy accounted for (N)

c_f coefficient of friction

A_g area of a ridge keel making contact with sea floor (m^2)

γ ratio of ridge keel depth to sail height ($H_k/H_s = 4.4$)

H_k ridge keel height (m)

H_s ridge sail height (m)

w_g water depth at ridge grounding (m)

α_k angle of the ridge keel (°)

l_g length of contact between ridge keel and sea floor (m)

α_s angle of the ridge sail (°)

F_{sb} force due to friction between ridge keels and the sea floor (N)

n_g number of grounded ridges across a profile of landfast ice

$\overline{D}_g$ average degree of grounding of a landfast ice cover

τ_k shear strength of a grounded ridge (Pa)

c cohesion strength of a grounded ridge (Pa)

σ_n normal stress acting on a failure surface (Pa)

θ angle of friction (°)

σ_t tensile stress on landfast ice (Pa)

σ_f flexural stress on landfast ice (Pa)

W_b weight above buoyancy of ice extension beyond grounded ridges (N)

l length between crack and location of load application (m)

L_E length between grounded ridges and ice edge (m)

Δw_d changes in sea level (m)

h roughness height of a surface feature (m)

λ wavelength (m)

Ψ local grazing angle (°)

E_I divergence/convergence

u_x ice velocity in x direction (m/s)

u_y ice velocity in y direction (m/s)

References

Banke, E.G., and S. D. Smith (1973), Wind stress on arctic sea ice, Journal of Geophysical Research, 78 (33), p. 7871-7883.

Brigham, L.W. (2007), Thinking about the Arctic's future: Scenarios for 2040, The Futurist, 41, p. 27-34.

Cassano, E., J. Cassano, and M. Nolan (2011), Synoptic weather pattern controls on temperature in Alaska, Journal of Geophysical Research, 116, D11108.

Coon, M.D., G.A. Maykut, R.S. Pritchard, D.A. Rothrock, A.S. Thorndike (1974), Modeling the pack ice as an elastic-plastic material. AIDJEX Bulletin, 24, p. 1-105.

Croasdale, K., S. Bruneau, D. Christian, G, Crocker, J. English, M. Metge, and R. Ritch (2001), In-situ measurements on the strength of first-year ice ridge keels, 16th International Conference on Port and Ocean Engineering Under Arctic Conditions, Ottawa, Canada, August 12-17, 2001, 3, p. 1445-1454.

Drobot, S., and J. Maslanik (2003), Interannual variability in summer Beaufort Sea ice conditions: Relationship to winter and summer surface atmospheric variability, Journal of Geophysical Research, 108, C7, 3233.

Druckenmiller, M., H. Eicken, M. Johnson, D. Pringle, and C. Williams (2009), Toward an integrated coastal sea-ice observatory: System components and a case study at Barrow, Alaska, Cold Regions Science and Technology, 56, p. 61-72.

Druckenmiller, M. (2011), Alaska shore fast ice: Interfacing geophysics with local sea ice knowledge and use, PhD Thesis, University of Alaska Fairbanks.

Eicken, H., A.L. Lovecraft, M. Druckenmiller (2009) Sea-ice system services: A framework to help identify and meet information needs relevent for arctic observing networks, Arctic, 62 (2), p. 119-136.

Eicken, H., M. Kaufman, I. Krupnik, P. Pulsifer, L. Apangalook, P. Apangalook (in press 2013), Developing a framework and database for community sea-ice observations for multiple users, Polar Geography.

Feltham, D.L. (2008). Sea ice rheology. Annual Review of Fluid Mechanics, 40, p. 91-112.

Gearheard, S., W. Matumeak, I.Angutikjuaq, J. Maslanik, H. Huntington, J. Leavitt, D. Matumeak Kagak, G.Tigullaraq, and R. Barry (2006), "It's Not that Simple": A Collaborative Comparison of Sea Ice Environments, Their Uses, Observed Changes, and Adaptations in Barrow, Alaska, USA, and Clyde River, Nunavut, Canada, AMBIO, 35 (4), p. 203-211.

George, J.C., H. Huntington, K. Brewster, H. Eicken, D. Norton, and R. Glenn (2004), Observation on shorefast ice dynamics in Northern Alaska and the responses of the Iñupiat hunting community, Arctic, 57 (4), p. 363-374.

Gray, J.M.N.T. and L.W. Morland (1994), A two-dimensional model for the dynamics of sea ice. Philosophical Transactions: Physical Sciences and Engineering, 347

(1682), p. 219-290.
Guest, P., K. Davidson, J. Overland, and P. Frederickson (1994), Atmosphere-ocean interactions in the marginal ice zones of the Nordic seas, In: W. Smith, J. Grebmeir (Eds.), Arctic oceanography: Marginal ice zones and continental shelves, American Geophysical Union, Washington, p. 51-95.
Hewitson, B.C., and R.G. Crane (2002), Self-organizing maps: applications to synoptic climatology, Climate Research, 22, p.13-26.
Hibler III, W.D. (1986), Ice dynamics In: N. Untersteiner (Ed), The Geophysics of Sea Ice. Plenum Press, New York, NY, p. 577-640.
Horner, R., and G. Schrader (1982), Relative contributions of ice algae, phytoplankton, and benthic microalgae to primary production in nearshore regions of the Beaufort Sea, Arctic, 35 (4), p. 485-503.
Johnson, W. (1989), Current response to wind in the Chukchi Sea: A regional coastal upwelling event, Journal of Geophysical Research, 94 (C2), p. 2057-2064.
Kalnay *et al.*,The NCEP/NCAR 40-year reanalysis project, Bull. Amer. Meteor. Soc., 77, 437-470, 1996.
Kohonen, T. (1995), *Self-Organizing Maps,* Springer, New York.
Leppäranta, M. (2005), The Drift of Sea Ice. Praxis Publishing, Chichester, UK, 266 pp.
Lewis, E., B. Currie, and S. Haykin (1987), Detection and Classification of Ice, Research Studies Press, Letchworth, Hertfordshire, England, 325 pp.
Mahoney, A., H. Eicken, L. Shapiro, and T. Grenfell (2004), Ice motion and driving forces during a spring ice shove on the Alaskan Chukchi coast, Journal of Glaciology, 50 (169), p. 195-207.
Mahoney, A., H. Eicken, L. Shapiro, and A. Graves (2005), Defining and locating the seaward landfast ice edge in northern Alaska, Proceedings of the 18th International Conference on Port and Ocean Engineering under Arctic conditions, POAC ’05, Volume 3, Potsdam, N.Y., June 26-30, 2005.
Mahoney, A., H. Eicken, A. Graves-Gaylord, and L. Shapiro (2007a), Alaska landfast sea ice: Links with bathymetry and atmospheric circulation, Journal of Geophysical Research, 112, C02001 p. 1-18.
Mahoney, A., H. Eicken, and L. Shapiro (2007b), How fast is landfast sea ice? A study of the attachment and detachment of nearshore ice at Barrow, Alaska, Cold Regions Science and Technology, 47, p. 233-255.
McBean, G. (1986), The atmospheric boundary layer. In: N. Untersteiner (Ed), The Geophysics of Sea Ice. Plenum Press, New York, NY, p. 283-338.
McPhee, M. (1979), The effect of oceanic boundary layer on the mean drift of pack ice: application of a simple model, Journal of Physical Oceanography, 9(2), p. 233-255.
McPhee, M. (1986), The upper ocean, In: N. Untersteiner (Ed), The Geophysics of Sea Ice. Plenum Press, New York, NY, p. 339-394.

Norton, D., and A. Graves Gaylord (2004), Drift velocities of ice floes in Alaska's Northern Chukchi Sea flaw zone: Determinants of success by spring subsistence whalers in 2000 and 2001, Arctic, 57 (4), p. 347-362.

Nuber, A., L. Rabenstein, J.A. Lehmann-Horn, M. Hertrich, S. Hendricks, A. Mahoney, and H. Eicken (2013), Water content estimates of a first-year sea ice pressure ridge keel from surface nuclear magnetic resonance tomography, Annals of Glaciology, 56(64), p. 33-43.

Petrich, C., H. Eicken, J. Zhang, J. Krieger, Y. Fukumachi, and K. Ohshima (2012), Coastal landfast sea ice decay and breakup in northern Alaska: Key processes and seasonal prediction, Journal of Geophysical Research, 117, C02003, 19 pp.

Reimnitz, E., and D. Maurer (1979), Effects of storm surges on the Beaufort Sea Coast, Northern Alaska, Arctic, 32 (4), p. 329-344.

Reimnitz, E., D. Dethleff, and D. Nürnberg (1994), Contrasts in Arctic shelf sea-ice regimes and some implications: Beaufort Sea vs Laptev Sea, Marine Geology, 119 (3-4), p. 215-225.

Reusch, D., R. Alley, and B. Hewitson (2005), Relative performance of self-organizing maps and principal component analysis in pattern extraction from synthetic climatological data, Polar Geography, 29 (3), p. 188-212.

Reynolds, M., C. Pease, J. Overland (1985), Ice drift and regional meteorology in the southern Bering Sea: Results from MIZEX West, Journal of Geophysical Research, 90, C6, p. 11967-11981.

Richardson, A., C. Risien, and F. Shilling (2003), Using self-organizing maps to identify patterns in satellite imagery, Progress in Oceanography, 59, p.223-239.

Rohith MV, C. Kambhamettu, J. Jones, and H. Eicken (2013), Extracting quantitative information on coastal ice dynamics and ice hazard events from marine radar digital imagery, Transactions on Geoscience and Remote Sensing, Transactions on Remote Sensing and Geosciences, 51 (5), p. 2556-2570.

Serreze, M.C., M.M. Holland, and J. Stroeve (2007), Perspectives on the Arctic's shrinking sea-ice cover, Science, 315, p. 1533-1536.

Shapiro, L. (1975), A preliminary study of the formation of landfast ice at Barrow, Alaska, Geophysical Institute Report UAG-R(235), Geophysical Institute, University of Alaska Fairbanks, Fairbanks, Alaska, 44 pp.

Shapiro, L., and R. Metzner (1987), Coefficients of friction of sea ice on beach gravel. In: L. Shapiro, P. Barnes, A. Hanson, E. Hoskins, J. Johnson, and R. Metzner (Eds.), Mechanical properties of sea ice deformation in the near shore zone, OCSEAP Final Report, Research Unit 265, p. 520-527, U.S. Department of Commerce, NOAA.

Shapiro, L. and R. Metzner (1989), Nearshore ice conditions from radar data, Point Barrow area, Alaska, Geophysical Institute Report UAG-R(312), Geophysical Institute, University of Alaska Fairbanks, Fairbanks, Alaska, 43 pp.

Sprenke, J., S. Gill, J. Kent, and M. Zieserl (2011), Tides under the ice: Measuring water levels at Barrow Alaska 2008-2010, NOAA Technical Report NOS CO-OPS 062, 69 pp.

Stewart, R. (2008), Introduction to Physical Oceanography, Open Source Textbook (http://oceanworld.tamu.edu/resources/ocng_textbook/contents.html), 353 pp.

Thorndike, A. (1986), Kinematics of sea ice, In: N. Untersteiner (Ed), The Geophysics of Sea Ice, Plenum Press, New York, NY, p. 489-549.

Thorndike, A., and R. Colony (1982), Sea ice motion in response to geostrophic winds, Journal of Geophysical Research, 87 (C8), p. 5845-5852.

Timco, G., and R. Burden (1997), An analysis of the shapes of sea ice ridges, Cold Regions Science and Technology, 25, p. 65-77.

Timco, G. (2008), Why does ice fail the way it does?, Proceedings of the 19th IAHR Symposium on Ice, Volume 2, p. 557-577, Vancouver, B.C., Canada, July 6-11, 2008.

Tremblay, L., and M. Hakakian (2006),Estimating the Sea Ice Compressive Strength from Satellite-Derived Sea Ice Drift and NCEP Reanalysis Data, Journal of Physical Oceanography, 36, p. 2165-2172.

Vesanto, J., J. Himberg, E. Alhoniemi, and J. Parhankangas (2000), Self-Organizing Map in Matlab: the SOM Toolbox, Updated version published in *Proceedings of the Matlab DSP Conference 1999*, p. 35-40, Espoo, Finland, November 1999.

Weingartner, T., D. Cavalieri, K. Aagaard, and Y. Sasaki (1998), Circulation, dense water formation, and outflow on the Northeast Chukchi shelf, Journal of Geophysical Research, 104 (C4), p. 7647-7661.

Weingartner, T., S. Danielson, J. Kasper, S. Okkonen (2009), Circulation and water property variations in the nearshore Alaskan Beaufort Sea (1999-2007), U.S. Department of the Interior, Minerals Management Service, Alaska Outer Continental Shelf Region, Anchorage Alaska, 168pp.

Wilson, K., J. Falkingham, H. Melling, and R. De Abreu (2004), Shipping in the Canadian Arctic-Other possible climate scenarios, Proceedings of 2004 IEEE International Geoscience and Remote Sensing Symposium, 2004, IGARSS ’04, III, p. 1153-1156.